[AMERICAN JOURNAL OF SCIENCE, VOL. 295, JUNE, 1995, P. 639–696]

American Journal of Science

JUNE 1995

THE FORMATION OF UNCONFORMITY-TYPE URANIUM ORE DEPOSITS 2. COUPLED HYDROCHEMICAL MODELING

JEFF P. RAFFENSPERGER* and GRANT GARVEN**

ABSTRACT. Circulation of deep groundwater is thought to have formed unconformity-type uranium ore deposits of Middle Proterozoic age such as those found in the Athabasca Basin of Canada and the McArthur Basin of Australia. Diagenesis and hydrothermal alteration accompanying ore formation probably occurred as oxidizing, uranium-bearing meteoric groundwater migrated through thick sandstone aquifers, precipitating uraninite at a stable redox interface near the unconformity between the sandstones and underlying metamorphic basement. Reducing conditions result from hydrothermal alteration of graphite, producing methane that moves upward through basement fault structures. Strong alteration, including sericitization and chloritization of the host lithologies, is closely related to the formation of these high-grade uranium ore deposits. Virtually all the deposits demonstrate similar paragenetic patterns—besides chlorite and mica, quartz precipitation and dissolution, pyrite precipitation, and several episodes of hematite formation and dissolution. A series of two-dimensional numerical calculations is presented in this paper to evaluate the paleohydrology and transient behavior of ore formation. The numerical simulations are based on fully coupled solutions to the equations for variable-density groundwater flow, advective and conductive heat transport, and multicomponent solute transport for reactive porous media in complex sedimentary basins. A finite element approach is used to solve the governing transport equations. The nonlinear reactive flow problem is solved in two dimensions using a predictor-corrector algorithm, for which local chemical equilibrium is assumed. A major goal of this work was to develop a general-purpose simulation code for reactive flow research, such that the diagenetic-hydrothermal concept of uranium ore formation could be quantitatively tested and evaluated.

Numerical simulations of generic cross sections and a sensitivity study of the reactive flow problem indicate that thermally-driven free convection of uranium-bearing saline groundwater (flow rates of about 1 m/yr) will precipitate uraninite in the vicinity of the unconformity between basin sandstones and basement graphite schists. Source concentrations of total aqueous uranium in the 20 to 30 ppm range probably were transported as uranyl-chloride complexes under moderately oxidizing conditions. Flow rates and uranium concentrations were suffi-

* Department of Environmental Sciences, University of Virginia, Charlottesville, Virginia 22903.

** The Morton K. Blaustein Department of Earth & Planetary Sciences, The Johns Hopkins University, Baltimore, Maryland 21218.

cient to produce large ore deposits near the unconformity within 0.1 to 1.0 Ma. Basement permeability and redox potential exert a strong control on the localization of ore deposition. The high permeability of a graphitic fracture zone within the basement and a chemical contrast between that zone and adjacent basement helped focus deep groundwater flow and mass transport up through the fracture zone and created a stationary redox front at the unconformity. Changes in bulk rock composition associated with alteration halos around the ore deposits result from mass transport through temperature gradients and across compositional boundaries. The modeling results indicate that in order to achieve observed patterns of ore mineralization and alteration, the graphitic fracture zone and zone of upward groundwater flow must coincide in space. Although other hydrodynamic scenarios were modeled, the free convection flow system appears to best replicate field observations for both alteration and ore mineralization.

INTRODUCTION

Some of the world's richest known uranium deposits are found in northern Saskatchewan, Canada, and in the Northern Territory, Australia. These deposits are Middle Proterozoic in age and are associated with unconformities beneath large intracratonic sedimentary basins (table 1). According to the diagenetic-hydrothermal model proposed for the formation of these deposits (Hoeve and Sibbald, 1978), oxidizing uranium-bearing meteoric waters circulate within permeable basin sandstones, precipitating uraninite at a stable redox interface near the unconformity. The uranium is thought to have been transported as soluble uranyl-carbonate complexes (McLennan and Taylor, 1979). Reducing conditions may have resulted from hydrothermal alteration of basement graphite, producing methane that moved upward through fault structures associated with the graphite-bearing schist. In addition, faulted basement structures are considered crucial in localizing uranium mineralization.

Although the diagenetic-hydrothermal concept has been the subject of qualitative models (Hoeve and Quirt, 1984), no earlier attempt was made to quantify the processes leading to ore formation. Such a model is necessary in order to resolve several important questions: (1) What factors led to the observed localization of uranium mineralization, and at what rate did mineralization occur? (2) What hydrochemical factors controlled formation of the alteration halo surrounding uranium mineralization?

Quantitative study of the chemical and hydrologic processes involved in geologic phenomenon such as the formation of sediment-hosted ore bodies has generally followed two paths. Hydrologic transport models are used to predict the fate of non-reactive solutes and evaluate the impact of transport phenomena such as advection, dispersion, diffusion, and the influence of initial and boundary conditions and properties of the medium. If the fluid is not moving but subject to changes in chemical composition as a result of water-rock interaction, chemical

TABLE 1

Features of Australian and Canadian unconformity-type uranium deposits

Deposit	Size (tons)[1]	Grade (%)[1]	Age (Ma)	Alteration	Graphite Content (wt. %)
ALLIGATOR RIVERS					
Jabiluka	227,000	0.30	1614±132[2] 1437±40[3]	chlorite, white mica, tourmaline, apatite, hematite, quartz[16]	
Ranger	147,000	0.20-0.30	1600-1750[2] 1737±20[3]	chlorite, quartz, pyrite[18]	
Koongarra	14,300	0.30	1600-1650[2]		
Nabarlek	13,200	1.85	1616±50[2]	white mica, Mg-chlorite, hematite[17]	
ATHABASCA BASIN					
Cigar Lake	121,000	12.2	1341±26[5]	illite, chlorite, hematite[14]	5-10[14]
Key Lake	75,000	2.35	1350±4[6] 1406±45[9]	kaolinite, chlorite, quartz, siderite, calcite[11]	25-45[11]
Midwest Lake	21,000	1.90	1328±17[10]	chlorite, sericite, muscovite[4]	
Collins Bay	20,000	0.25	1281±80[8]	illite, chlorite, hematite[15]	
Rabbit Lake	20,000	0.45		chlorite, dolomite, quartz, tourmaline[12]	
Dawn Lake	11,000	1.00		clays, hematite[15]	
McClean Lake	11,000	1.80	~1320[7]	illite, chlorite, hematite[13]	25-45, up to 80[13]

KEY

[1] Wilde (1988).
[2] Maas (1989).
[3] Ludwig and others (1987).
[4] Ayres and others (1983).
[5] Philippe and Lancelot (1988).
[6] Trocki and others (1984).
[7] Bray and others (1987).
[8] Fryer and Taylor (1984).
[9] Carl and others (1988).
[10] Baadsgaard, Cumming, and Worden (1984).
[11] Dahlkampt (1978).
[12] Hoeve and Sibbald (1978).
[13] Bray, Spooner, and Longstaffe (1988).
[14] Bruneton (1987).
[15] Tremblay (1982).
[16] Nutt (1989).
[17] Wilde and Wall (1987).
[18] Hegge and Rowntree (1978).

equilibrium models may be used to determine the speciation and assess the influence of variations in pH, redox potential, temperature, or pressure. Non-equilibrium thermodynamics have also been incorporated into these models, allowing "reaction paths" to be simulated (Helgeson, 1968; Helgeson and others, 1970). Only recently have models that include transport of multicomponent reactive species been developed and applied to problems such as contaminant migration in the subsurface, sedimentary diagenesis, and ore formation (Miller and Benson, 1983; Cederberg, Street, and Leckie, 1985; Ortoleva and others, 1987; Ague and Brimhall, 1989; Liu and Narasimhan, 1989; Steefel and Lasaga, 1992, 1994; Lichtner and Biino, 1992).

A major goal of this study is the development of a hydrologic-geochemical transport model of unconformity-type uranium mineralization. In this paper, the second of two parts, numerical calculations are presented for coupled groundwater flow, heat transport, and multicomponent reactive solute transport in a hypothetical sedimentary basin. The objective of this work is to examine the hypothesis that free convection was responsible for the formation of these deposits and their associated alteration halos. Hydrogeologic aspects of free convection within thick sandstone sequences were treated in part 1 (1995, p. 581–636).

GEOLOGIC SETTING OF THE ORE DEPOSITS

1. East Alligator River region, Australia.—The major uranium deposits of the East Alligator River region (Koongarra, Jabiluka, Ranger, and Nabarlek) contain approx 400,000 tons of U_3O_8 (Wilde, 1988). These deposits are found along the eastern edge of the Pine Creek Geosyncline (Plumb and others, 1981), where the Middle Proterozoic (1600-900 Ma) platform sediments of the McArthur Basin unconformably overlie Archean-Early Proterozoic gneisses and metasediments of the Pine Creek Geosynclinal sequence (Needham, Stuart-Smith, and Page, 1988, fig. 1).

Uranium mineralization at Koongarra, Jabiluka, Ranger, and Nabarlek is confined to brecciated carbonaceous and chlorite schists of the Lower Cahill Formation (Needham and Stuart-Smith, 1976), below the unconformable contact with the overlying Kombolgie sandstone at the northwestern edge of the McArthur Basin. Primary mineralization typically consists of uraninite and massive amorphous pitchblende and is strongly associated with chloritization (magnesium metasomatism) of the host rock (Gustafson and Curtis, 1983) and sericitization of carbonate and carbonaceous (graphite) schist. The major gangue minerals are chlorite, quartz, and sericite, and sulfides, such as pyrite, chalcopyrite, and galena, are associated with the ore deposits (Hegge and Rowntree, 1978). Hematite is also commonly associated with the ores but is thought to post-date ore formation (Ewers, Ferguson, and Donnelly, 1983). Bleaching (hematite removal) occurs at Jabiluka (Gustafson and Curtis, 1983).

An intense hydrothermal alteration halo surrounds ore mineralization at Nabarlek, which extends more than 1 km from the ore (Wilde and Wall, 1987). Ore deposition is associated with a small zone of quartz dissolution and chlorite precipitation. Surrounding the ore zone is an inner halo (fig. 2), which is defined by white-mica, chlorite, and hematite precipitation, and an outer halo, consisting of quartz, chlorite, and white-mica precipitation and minor pyrite precipitation (Wilde and Wall, 1987).

Perhaps the best-studied of the Australian deposits is the Koongarra ore body (Foy and Pederson, 1975; Ewers and Ferguson, 1980; Snelling, 1980). Typical of unconformity-type uranium deposits in Australia as well as Canada, the ore deposit has a characteristic shape (shown in cross section in fig. 3) which is narrow (50-100 m) but which extends up to 450

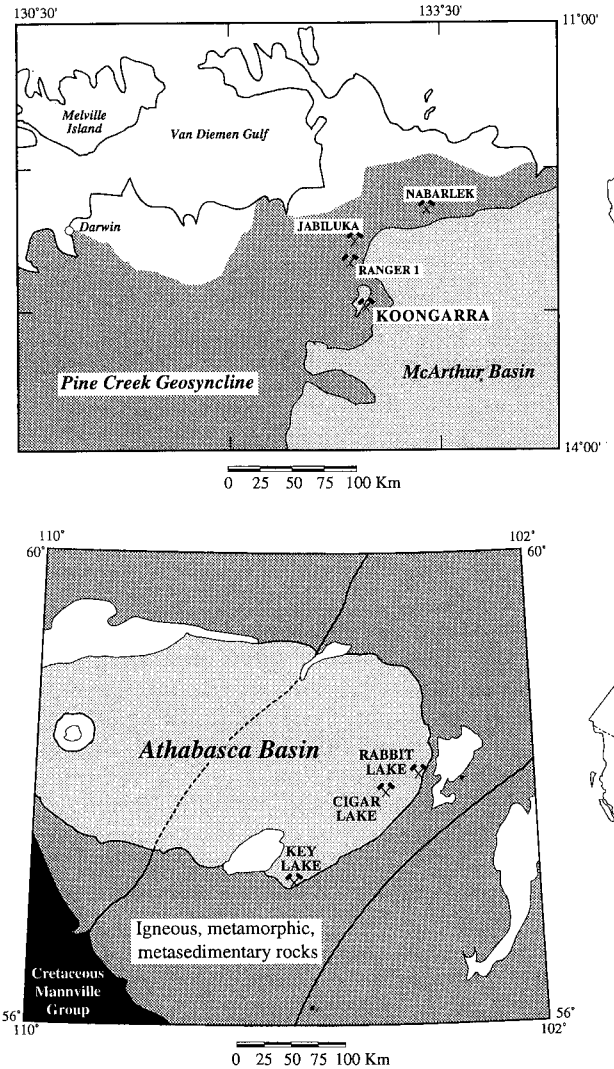

Fig. 1. Location of uranium deposits within the Alligator Rivers region of Australia (top) and the Athabasca Basin of Canada (bottom).

m along strike. In general, deposits are generally confined to widths of 50 to 300 m but may be up to 3400 m in length (Wilde, 1988). This gives the deposits a characteristic "cigar" shape. Primary mineralization at Koongarra is surrounded by an alteration halo consisting of pervasive chloriti-

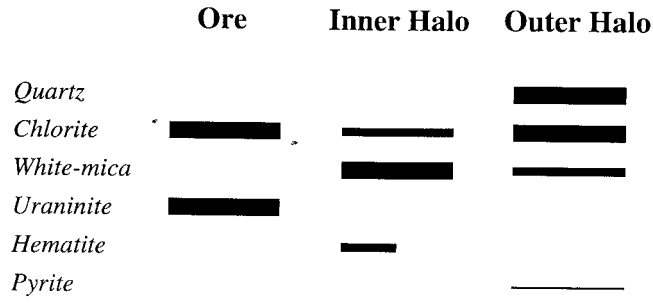

Fig. 2. Paragenesis diagram, Nabarlek deposit. Line widths correspond to the relative amount of material precipitated. Modified from Wilde and Wall (1987).

zation and quartz removal. Uraninite and pitchblende have subsequently been altered to form uranyl silicates and later weathered to form phosphates (Snelling, 1980; Isobe, Murakami, and Ewing, 1992). Recent transport of uranium by the present-day groundwater flow system is thought to be responsible for the dispersed plume of uranium extending some 50 m away from the altered zone.

II. Athabasca Basin, Canada.—Major unconformity-type uranium deposits are found at Rabbit Lake, Cigar Lake, Key Lake, and other locations at the eastern and southeastern edge of the Athabasca Basin (fig. 1). The general history of the region and the relationship between various phases of geologic activity and major uranium mineralization events have been summarized by Bell (1981).

The eastern perimeter of the Athabasca Basin unconformably overlies the Aphebian metasediments and migmatites of the Daly Lake Group within the Wollaston Lake Fold Belt (Money, 1968). The major uranium deposits of the region are found predominantly within metasedimentary rocks, often flanking Archean granitic domed cores (Dahlkamp, 1978). As is the case for the Australian deposits, mineralization is strongly associated with the unconformity at the base of the Athabasca Group sedimentary rocks but, unlike those deposits, may extend upward into the overlying sandstones (Tremblay, 1982).

The Late Aphebian-Early Helikian Hudsonian orogeny (about 1850 Ma) folded and metamorphosed the host sediments (Cumming and Scott, 1976; Hoffman, 1989), which were later uplifted and eroded. Deposition of Athabasca sediments followed at approx 1450 Ma, with major primary uranium mineralization occurring some 100 to 150 Ma later (Bray and others, 1987).

The major Athabascan uranium deposits are strikingly similar to their Australian counterparts (table 1) and are characterized by their (Hoeve and Quirt, 1984; Marmont, 1987): (1) association with faulted basement structures and a paleoweathering surface; (2) stratigraphic proximity to a major unconformity; (3) shape, high grade, and primary

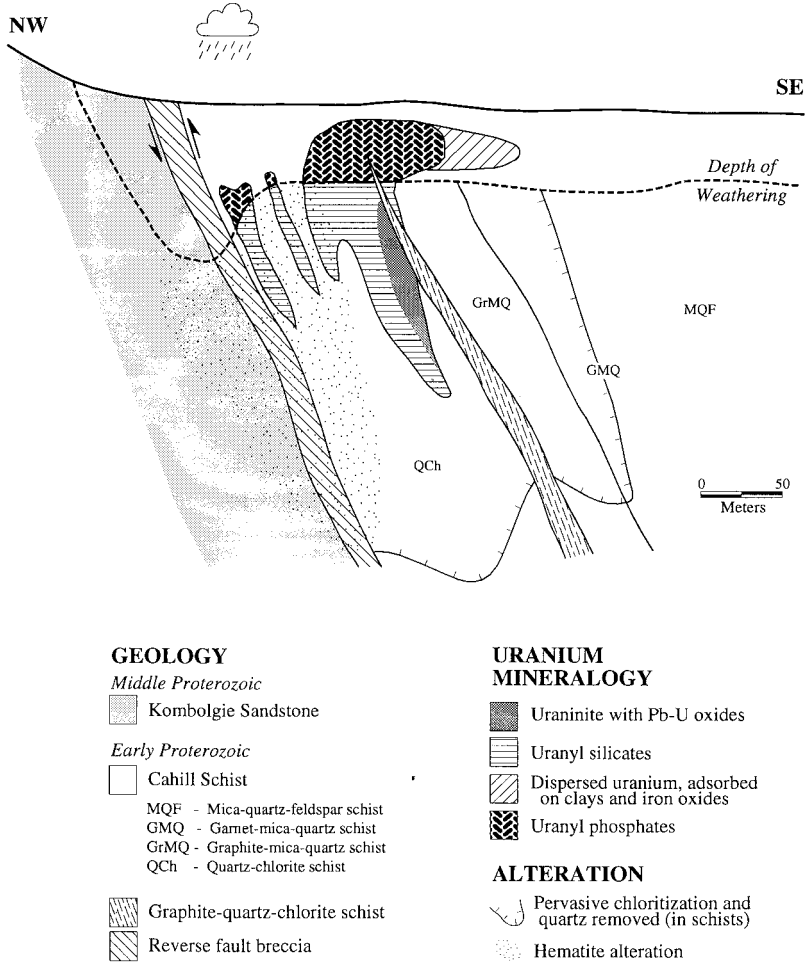

Fig. 3. Section across the Koongarra deposit. No vertical exaggeration. After Snelling (1980).

mineralogy; (4) association with carbonate and/or carbonaceous rocks; and (5) Middle Proterozoic age.

The Gaertner and Deilmann (fig. 4) ore bodies at Key Lake were described by Dahlkamp (1978). These ore bodies are separate but follow the trend of basement faulting and are nearly 5 km in combined length. Mineralization is associated with graphite-bearing basement rocks but extends up into the overlying Athabasca Group sandstone. Intense hydrothermal alteration surrounds primary mineralization and has affected both basement and basin rocks. Gangue minerals include kaolin-

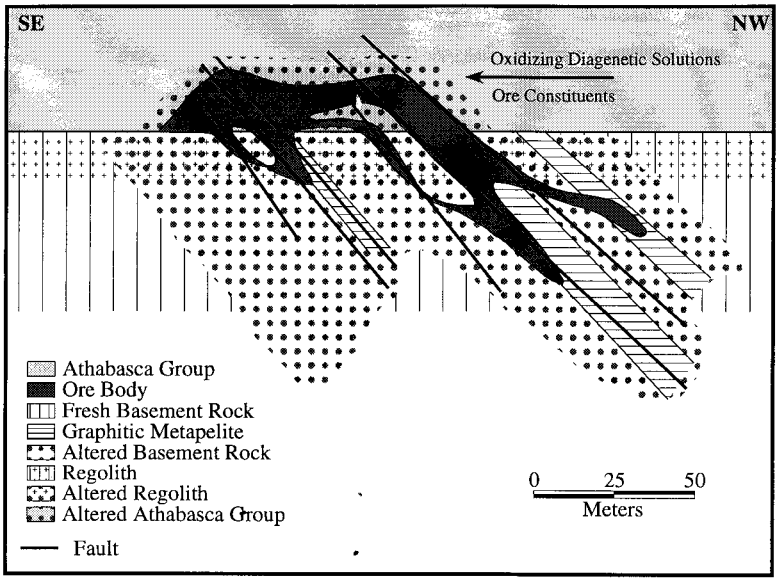

Fig. 4. Section across the Deilmann ore body at Key Lake. After Dahlkamp (1978) and Hoeve and Sibbald (1978).

ite, chlorite, quartz, siderite, calcite, and others (Dahlkamp, 1978; Ruhrmann, 1987). The alteration halo is distinctly zoned, with strong chloritization, as well as hematite and pyrite precipitation, near the ore. Illite and hematite relicts are found in the outer portion of the halo, and quartz overgrowths occur throughout the altered rocks (Ruhrmann, 1987).

Host rock alteration at the Midwest Lake deposit occurs along the strike of the ore-bearing fault zone, extending for at least 5 to 6 km along the fault zone. Faulting coincides with the trace of graphite-rich metapelites within the basement gneiss (Hoeve, 1984). Mineralization extends for approx 500 m along the strike of the fault zone, and the ore zone has a maximum width of 150 m and a maximum thickness of 36 m (Ayres and others, 1983). Hoeve (1984) distinguished two stages of host rock alteration: (1) clay alteration under oxidizing conditions (hematite stable); and (2) younger superimposed bleaching under reducing conditions which resulted in hematite removal. Clay alteration is accompanied by quartz dissolution producing a friable zone which extends upward, well into the basin sediments.

The Cigar Lake deposit (fig. 5) provides a good example of the strong concentric zonation of alteration associated with the unconformity-type uranium deposits. The ore itself occurs as a flat, elongated body extending over a length of 2150 m, with a maximum width and thickness

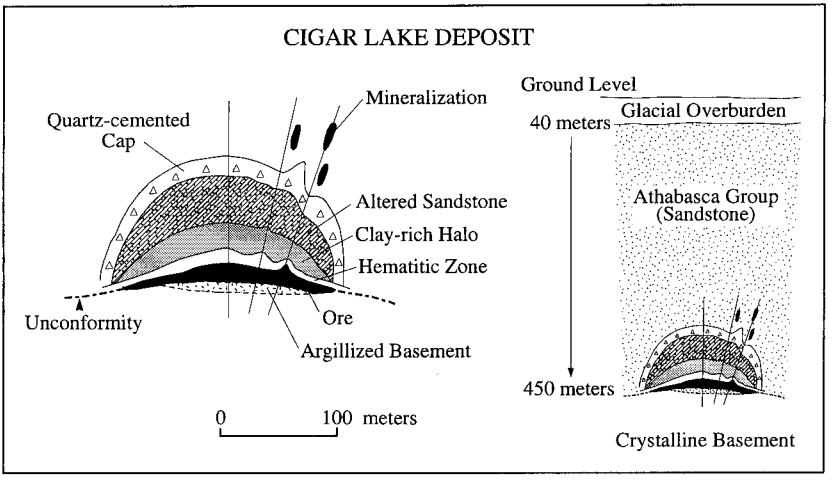

Fig. 5. Section across the Cigar Lake deposit. No vertical exaggeration. After Percival and Kodama (1989).

of 100 and 20 m, respectively (Bruneton, 1987). Most of the ore is hosted by Athabasca Group sandstones, and the surrounding alteration halo consists of (outward from the ore): a hematite cap; illite, with massive quartz dissolution; and quartz overgrowths. Pyrite fills small veins within the basement rocks.

GEOCHEMICAL CONCEPTS OF ORE GENESIS

Early theories concerning the genesis of these deposits considered the following models: a supergene origin (Derry, 1973; Langford, 1974, 1977, 1978); primary hypogene with supergene or hydrothermal enrichment (Dahlkamp, 1978, 1979); and hydrothermal (Ryan, 1979). Others have suggested more complex, polygenetic models of ore formation (Tremblay, 1982; Marmont, 1987). In general, these early models were later found to be inadequate as more accurate information on ages of mineralization and hydrothermal fluid composition became available.

Based on more detailed and recent data on ages of mineralization and associated alteration, as well as fluid inclusion data, many workers currently favor the diagenetic-hydrothermal model for the formation of unconformity-type uranium deposits (Hoeve and Sibbald, 1978). According to this theory, oxidizing, uranium-bearing meteoric waters move downward through basinal sands, precipitating uraninite at a stable redox interface in the vicinity of the unconformity (fig. 6). The uranium is thought to have been derived from the sandstone and interbedded volcanics and transported as soluble uranyl-carbonate complexes (McLennan and Taylor, 1979). Reducing conditions are conjectured to result from hydrothermal alteration of graphite, producing methane which

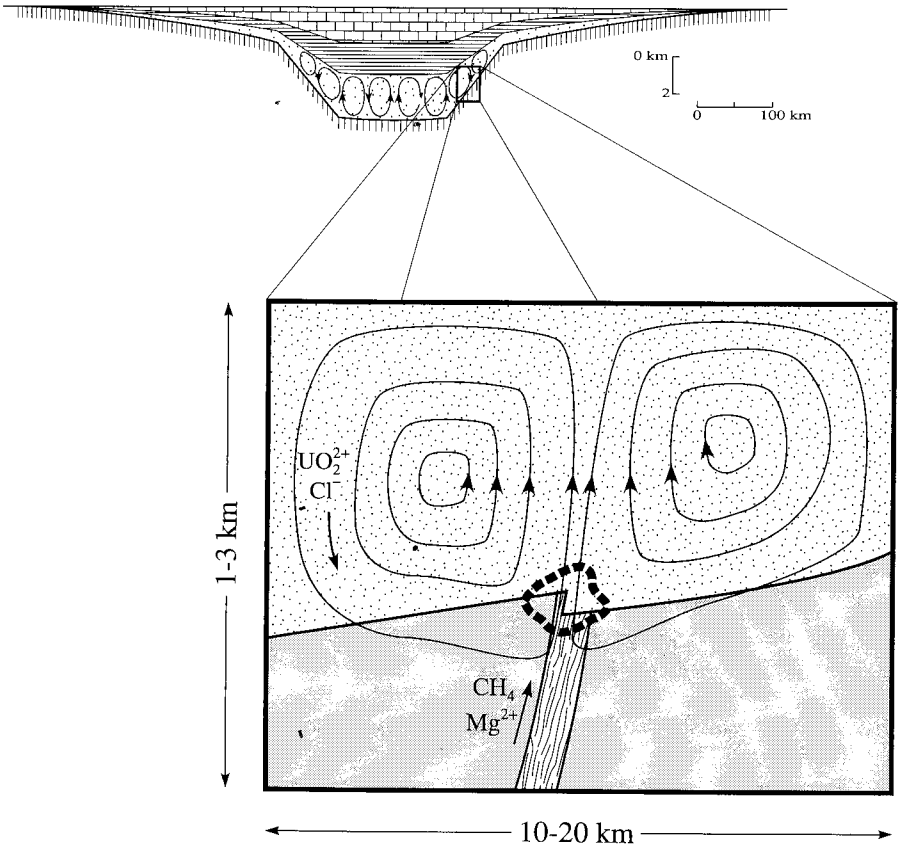

Fig. 6. Conceptual model of unconformity-type uranium mineralization by basinal brines.

moves upward through basement fault structures associated with the graphite-bearing schist.

Hoeve and Quirt (1984) suggested that free convection in a thick sandstone sequence could explain the diagenetic features associated with these deposits. Based on observations of clay mineral diagenesis within the Athabasca Basin, they described a geochemical model in which the ore was surrounded by a zone of secondary hematite precipitation and an outer halo of clay alteration and quartz dissolution. Several stages of mineralization were required to explain the observed patterns of alteration. However, ages of mineralization indicate reworking of these deposits after primary ore formation (Marmont, 1987).

Essential to this concept is the idea of a stationary redox front (Hoeve and Quirt, 1987), which is thought to be the result of hydrothermal

destruction of graphite. Kyser, Wilson, and Ruhrmann (1989) used carbon isotope data to argue that methane generation by graphite destruction was not responsible for reduction of uranium. They suggest that graphite played solely a hydromechanical role, by localizing basement faulting and fracturing, which enhanced local permeability thereby channeling mineralizing fluids. At the McClean deposit, however, graphite immediately beneath mineralization shows evidence of reaction, with pronounced depletion zones and recrystallization to a fine-grained soot (Bray, Spooner, and Longstaffe, 1988).

The question of the source of the mineralizing and reducing fluids has been another area of study. Hoeve and Quirt (1984, 1987) suggested that meteoric, basin-derived fluids penetrated the basement and transported reductant to the site of ore genesis. Kotzer and Kyser (1990a,b) have studied stable isotope systematics (H, O, C, S) within the basin and basement and proposed that the mineralizing fluid and reducing fluid were quite different and distinct, with the latter being derived from a deep basement source.

MATHEMATICAL MODEL

The methods used to calculate groundwater flow patterns and temperatures were described in part 1 (1995, p. 597) and are presented in detail in Raffensperger (1993). In this section we will describe only the development of the reactive multicomponent solute transport model.

The study of reactive multicomponent chemical transport has been undertaken by researchers in a variety of fields, such as chemical engineering, petroleum engineering, soil science, geochemistry, and hydrogeology. Due to the complexity of the problem, mathematical models are generally solved numerically and are usually custom-designed for a specific use. As a result, the majority of these efforts do not consider the full range of physical phenomena. Reviews may be found in Boast (1973), Rubin (1983), Grove and Stollenwerk (1987), Langmuir (1987), Mangold and Tsang (1991), and Raffensperger (ms).

A general mathematical statement for the transport of multiple reactive solutes by advection and dispersion due to steady flow in porous media may be written:

$$\nabla \cdot (\phi \mathbf{D} \nabla c_i) - \phi \mathbf{v} \cdot \nabla c_i = \frac{\partial \phi c_i}{\partial t} - \phi R_i \qquad i = 1, 2, \ldots, I \tag{1}$$

where $\mathbf{D}$ is the dispersion tensor (which includes the effects of both mechanical dispersion and diffusion), ϕ is the porosity, c_i is the mass concentration of species i, $\mathbf{v}$ is the average linear velocity, and R_i is the rate of addition of species i to the fluid by all reactions. R_i is negative if species i is removed from the fluid by adsorption or precipitation of solids. Theoretical derivations of eq (1) may be found in Boast (1973), Chu and Sposito (1980), Marle (1982), Nguyen and others (1982), and Rubin (1983).

Solution of the set of partial differential equations (1) requires knowledge of the flow field and the rate of addition to the fluid phase of each chemical species. If local equilibrium is assumed (Rubin, 1983), these rates are constrained by appropriate mass action expressions. Otherwise, kinetic rate expressions must be used. In either case, the transport relations are nonlinear.

Methods for numerically solving the coupled transport and chemical relations fall into two main categories. Direct methods incorporate chemical equilibrium or kinetic rate expressions directly in the transport equations, thereby solving both sets of equations simultaneously (Steefel and Lasaga, 1992). The earliest modeling efforts generally used direct coupling methods, but with simple chemistry and/or simplified flow fields. Many of these studies have examined ion exchange, following pioneering work by Rubin and James (1973). The CHEMTRN code (Miller and Benson, 1983) solves both sets of equations simultaneously and has undergone several revisions (Noorishad, Carnahan, and Benson, 1985; Carnahan, 1987).

Alternatively, consider that only the partial differential equations governing transport are field equations. The nonlinear algebraic equations describing chemistry (mass balance and mass action) are point equations (that is, they do not involve spatial derivatives). This suggests that the transport and chemistry relations may be posed independently and solved sequentially (Rubin, 1983). Sequential solution methods have become more common in recent years, since speciation codes exist that are easily coupled with available transport codes. In this approach, the mass transport and reaction equations are solved separately and sequentially, with iteration between the two solutions required to resolve the nonlinearities. Examples that make use of the sequential approach are provided by Walsh and others (1984) and Cederberg, Street, and Leckie (1985). Commonly these codes will incorporate existing external chemical speciation codes, such as MINEQL (Kirkner, Theis, and Jennings, 1984), or reaction path codes, such as PHREEQE (Sanford and Konikow, 1989) and EQ3/EQ6 (Ague and Brimhall, 1989). The difficulty in this approach is that these particular chemical submodels may require excessive amounts of computer time, thereby making them impractical for geologic-scale simulations.

Chemical components are here defined as linearly independent chemical entities, such that every non-component species can be uniquely represented as a combination of these components, yet no one component as a combination of other components. In addition, these components are defined to correspond to species in the aqueous phase, referred to as "component species" (Reed, 1982). The use of these components, rather than neutral species, elements, or oxides, reduces the computer storage requirements significantly (Helgeson and others, 1970). Furthermore, the total mass of a component defined in this manner will be reaction-invariant (Rubin, 1983).

TABLE 2

Governing equations for reactive solute transport

Conservation of Solute Mass in Flow System:

$$\nabla \cdot \left(\mathbf{D}\nabla \phi M^T_{c,aq}\right) - \mathbf{v} \cdot \nabla \phi M^T_{c,aq} = \frac{\partial \phi M^T_c}{\partial t}$$

Mass Balance in Chemical Subsystem:

$$M^T_{c,aq} = M_c + \sum_{s=1}^{\hat{s}} \tau_{cs} M_s$$

$$M^T_{c,sol} = \sum_{m=1}^{\hat{m}} \tau_{cm} M_m$$

$$M^T_c = M_c + \sum_{s=1}^{\hat{s}} \tau_{cs} M_s + \sum_{m=1}^{\hat{m}} \tau_{cm} M_m$$

Mass Action in Chemical Subsystem:

$$K = \prod_i a_i^{\nu_i}$$

ϕ	–	Porosity (fraction)
t	–	Time (yr)
$\mathbf{v}$	–	Average linear velocity (m/yr)
$\mathbf{D}$	–	Hydrodynamic dispersion tensor (m^2/yr)
c	–	Designates a component or aqueous component species
$\hat{c}$	–	Number of chemical components
s	–	Designates an aqueous complex or secondary aqueous species
$\hat{s}$	–	Number of aqueous complexed or secondary aqueous species
m	–	Designates a solid mineral species
$\hat{m}$	–	Number of precipitated or solid mineral species
aq	–	Subscript referring to the aqueous phase
sol	–	Subscript referring to the solid phase
M	–	Concentration (molarity)
M^T	–	Total concentration (molarity)
τ_{cm}	–	Composition coefficient (moles of component per formula weight)
τ_{cs}	–	Composition coefficient (moles of component per formula weight)
K	–	Equilibrium constant or solubility product
a_i	–	Equilibrium activity of the ith species
ν_i	–	Stoichiometric reaction coefficient for the ith species

We may make several observations based on the formulation of the general transport relation for components (table 2). The change in the total analytical concentration (M^T_c) of each component is due only to the hydrologic transport processes of advection and dispersion (including molecular diffusion); no nonlinear reaction terms are explicitly present. This is a direct result of the definition of conservative component and allows us to separate the transport relations and chemical relations. Each

transport equation is identical in form, and as such they can be solved sequentially. All other secondary dependent variables, that is, the concentrations of the complexes and minerals, may then be determined at each point within the flow domain.

For this study, the finite element method is used to solve the equations describing two-dimensional reactive multicomponent solute transport (table 2). Solution to the reactive transport problem is accomplished using a sequential approach, in which advection-dispersion transport equations are solved for each chemical component, followed by speciation at all nodes. Rather than iterating between the transport and chemical equilibrium equations within a time step, a two-step predictor-corrector scheme is used which decreases the computational effort without sacrificing accuracy (Raffensperger, ms). Local equilibrium is assumed, which is thought to be a valid approximation when space and time scales of interest are large (Knapp, 1989). The limitations of a local equilibrium approach for the simulation of problems involving mineral precipitation and dissolution have been discussed by several workers (Knapp, 1989; Phillips, 1991; Lichtner, 1992). In particular, determining a scale of interest for any given situation is problematic (Raffensperger, ms; Steefel, 1994, personal communication).

In summary, reactive solute transport is described by two coupled sets of equations: (1) a set of partial differential equations describing the transport of each chemical component, and (2) a set of nonlinear algebraic equations describing equilibrium chemistry, including acid/base and redox reactions. The transport equations are solved using the finite element method with a predictor-corrector time-stepping scheme (app. 1). This solution provides the distribution of total analytical concentrations (M_c^T). The actual distribution of species is determined by solving the set of nonlinear algebraic mass balance and mass action equations describing the distribution of mass amongst the various component species, secondary species and complexes, and solids. Details of the numerical procedure are given in Raffensperger (ms).

Various numerical methods exist for solving sets of nonlinear algebraic equations. Newton-Raphson iteration is one of the best-known and converges relatively rapidly, as long as adequate initial estimates are provided (Burden, Faires, and Reynolds, 1981; Press and others, 1986). The chemical submodel for this study uses Newton-Raphson iteration to solve the set of combined mass balance and mass action equations (table 2), which are written in a logarithmic form. A direct search optimization procedure (Walsh, 1983) is used to provide initial estimates.

Thermodynamic data used to calculate equilibrium constants for minerals are taken from Helgeson and others (1978), Berman (1988), and Sverjensky, Hemley, and D'Angelo (1991). Data for aqueous species are from Shock and Helgeson (1988) and Shock, Helgeson, and Sverjensky (1989). Data for aqueous uranium species and uranium minerals are

TABLE 3

Summary of chemical species. Note that fluid compositions may be described using the component species name, for example, total aqueous Fe^{3+}, even when most of that component occurs as a secondary species, for example, as Fe^{2+} under reducing conditions

Component Species (c_i)													
H_2O	OH^-	Na^+	K^+	Ca^{2+}	Mg^{2+}	UO_2^{2+}	Al^{3+}	Fe^{3+}	Cl^-	CO_3^{2-}	SO_4^{2-}	SiO_2^0	CH_4^0

Secondary Aqueous Species (s_i)						
H^+	O_2^0	HCl^0	CO_2^0	HCO_3^-	HSO_4^-	HS^-
H_2S^0	$HSiO_3^-$	$HFeO_2^-$	$NaOH^0$	$NaCl^0$	$NaHCO_3^0$	$NaHSiO_3^0$
KOH^0	KCl^0	KSO_4^-	$KHSO_4^0$	$CaCl^+$	$CaCl_2^0$	$CaCO_3^0$
$CaHCO_3^+$	$CaSO_4^0$	$MgOH^+$	MgO^0	$MgCl^+$	$MgCO_3^0$	$MgHCO_3^+$
U^{3+}	U^{4+}	UCl^{3+}	UCl_2^{2+}	$UHCO_3^{3+}$	$U(HCO_3)_2^{2+}$	UO_2^+
UO_2Cl^0	$UO_2Cl_2^-$	$UO_2HCO_3^0$	$UO_2(HCO_3)_2^-$	UO_2Cl^+	$UO_2Cl_2^0$	$UO_2CO_3^0$
$UO_2HCO_3^+$	$UO_2(HCO_3)_2^0$	$UO_2SO_4^0$	$UO_2HSO_4^+$	$AlOH^{2+}$	$AlCl^{2+}$	$AlCl_2^+$
$FeCl^{2+}$	Fe^{2+}	$FeOH^+$	FeO^0	$FeCl^+$	$FeCl_2^0$	$FeHCO_3^+$

Minerals (m_i)		
Halite [NaCl]	Albite [$NaAlSi_3O_8$]	Sylvite [KCl]
K-feldspar [$KAlSi_3O_8$]	Muscovite [$KAl_2(AlSi_3O_{10})(OH)_2$]	Calcite [$CaCO_3$]
Dolomite [$CaMg(CO_3)_2$]	Anhydrite [$CaSO_4$]	Anorthite [$CaAl_2Si_2O_8$]
Magnesite [$MgCO_3$]	Cordierite [$Mg_2Al_4Si_5O_{18}$]	Chlorite [$Mg_5Al(AlSi_3O_{10})(OH)_8$]
Uraninite [UO_2]	Rutherfordine [UO_2CO_3]	Kaolinite [$Al_2Si_2O_5(OH)_4$]
Hematite [Fe_2O_3]	Magnetite [Fe_3O_4]	Siderite [$FeCO_3$]
Pyrite [FeS_2]	Quartz [SiO_2]	Graphite [C]

from Grenthe and others (1990), although values for uranium complexes were determined using the methods described by Shock and Helgeson (1988) and Sverjensky (1987). The database for the chemical submodel consists of 70 aqueous species and 21 possible solids (table 3 and app. 2). A modified extended Debye-Hückel equation is used to determine activity coefficients, which provides an adequate geochemical approximation for NaCl brines up to 6 molal (Helgeson, Kirkham, and Flowers, 1981; Oelkers and Helgeson, 1990). Hydrogen is included as a component species to allow for variations in fluid pH. Redox state is determined by including two components (redox pair) containing the same element with different valences (CO_3^{2-} and CH_4^0) within the mass balance equations, rather than a hypothetical electron activity. The activity of water (a_{H_2O}) is assumed to be one, since variations are small for the range of conditions examined in this study, for example, at 150°C in a 2.5 molal NaCl solution, the activity of water is approx 0.92 (Helgeson, 1969).

RESULTS

In this section, we will present in detail the results of one simulation that documents mineralogical patterns accompanying 0.5 Ma of uraninite precipitation near an unconformity. The calculations assume a free convection flow system based on the analysis of coupled groundwater flow and heat transport presented in part 1. In addition, two other simulations will be presented briefly, in order to examine the possibility of different hydrologic systems and other starting compositions. Although more than 20 simulations were conducted in this study, in the interest of space many of these results cannot be given in detail but will be discussed where relevant.

I. *Free convection and the formation of an alteration halo.*—The first simulation considers a single flow cell in a section through a sedimentary basin which is characteristic of the domains considered in part 1. The numerical grid consists of 121 nodes, 200 triangular finite elements, and 4 hydrostratigraphic units (fig. 7): basement rock, a faulted "graphite" zone, overlying sandstone, and an upper confining unit. Discretization is more refined over the graphite unit, where we expect most of the reactive mass transport to occur. The bottom and sides are modeled as impermeable boundaries, the top surface is modeled as water table, a constant temperature of 20°C is assumed for the upper surface, and a basal heat flux of 80 mW/m^2 is applied across the bottom. Little is known about the thermal dispersion tensor (Mercer and Faust, 1979), especially at a basin scale, although thermal dispersion is thought to be important at this scale (Garven and Freeze, 1984). Therefore, values used here are the same as values of the solute dispersivity (Marsily, 1986). A constant salinity gradient of 0.0001 mass fraction/m depth is assumed, beginning at a depth of 1 km and reaching a maximum of 23 wt percent at a depth of 3.3 km. This salinity gradient is used in the calculations of variable-density groundwater flow, and we assume the salinity field is unaffected by the flow field.

Each hydrostratigraphic unit requires initial chemical compositions, which are given in tables 4 through 7. These tables summarize the aqueous compositions and volume fractions of minerals for each unit at a particular temperature. In actuality, these compositions vary slightly with temperature, because input constraints are given as total analytical concentrations (M_c^T) of the component species (table 3). The top and bottom boundaries are assigned constant compositions which are the same as their respective units. Longitudinal and transverse dispersivities are 300 and 30 m, respectively. These values are required for numerical reasons (to avoid numerical dispersion) and are comparable to values measured at a regional scale (Gelhar, Welty, and Rehfeldt, 1992), which result from heterogeneities that enhance fluid mixing.

We can briefly examine the starting compositions for the four units:

Unit 1—Basement (table 4), a quartz–muscovite–chlorite schist,

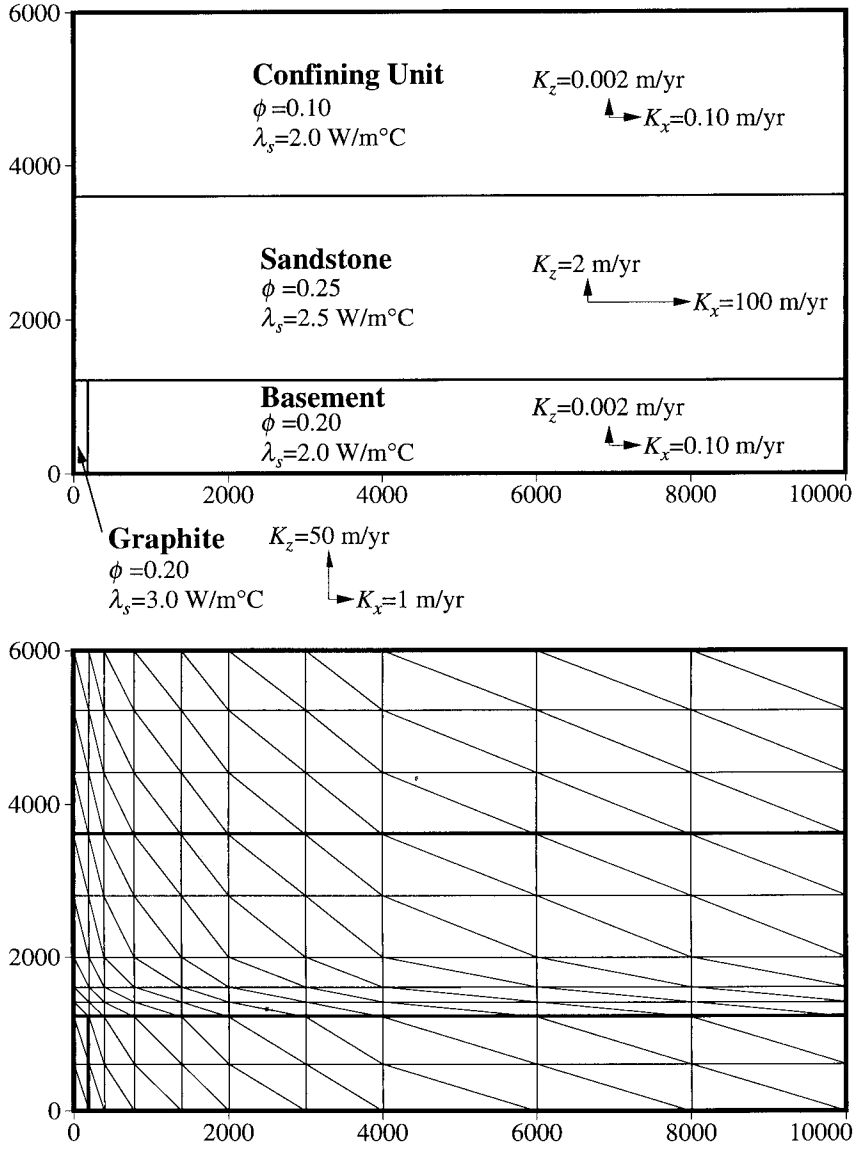

Fig. 7. Hydrostratigraphy, finite element mesh, and parameters for simulation of reactive solute transport due to free convection. Axes units are meters.

modeled on the Cahill schist. Moderately reducing and slightly acidic conditions are conjectured.

Unit 2—Graphite (table 5), which resembles the basement unit but contains 8.5 volume percent graphite and is more reducing. The

TABLE 4

Initial conditions for the basement unit

Temperature	150 °C
pH	4.541
E_H (volts)	−0.077
$p\varepsilon$	−0.922
$\log f_{O_2}$	−46.834
$\bar{I}$ (molarity)	2.579

Summary of the Aqueous Phase

Component Species	$M^T_{c,aq}$
Na^+	0.100
Ca^{2+}	0.853
K^+	0.163
Mg^{2+}	0.365
UO_2^{2+}	0.82×10^{-10}
Fe^{3+}	0.002
Cl^-	2.700
CO_3^{2-}	0.049
SO_4^{2-}	0.00056

Summary of the Solid Phase

Mineral	M_m	ϕM_m	Volume Fraction
K-feldspar	2.28	0.456	0.0494
Muscovite	11.55	2.310	0.3263
Dolomite	0.0004	0.00008	0.0000
Anhydrite	0.35	0.07	0.0032
Chlorite	0.127	0.025	0.0056
Uraninite	1.00×10^{-5}	0.20×10^{-5}	0.0000
Hematite	0.086	0.017	0.0005
Pyrite	0.027	0.005	0.0001
Quartz	91.51	18.296	0.4148
POROSITY			0.2000

concentration of aqueous methane is 0.25 moles/liter (≈4000 ppm), which is within the range of methane solubilities in NaCl brines at 150° to 200°C and 500 to 1000 bars (Hanor, 1987).

Unit 3—Sandstone (table 6), predominantly quartz, K-feldspar, and hematite, in equilibrium with a Na–Ca–Cl brine. Assumed to be the uranium source, an initial fluid composition of 1.0×10^{-4}

TABLE 5

Initial conditions for the graphite unit

Temperature	170 °C
pH	4.094
E_H (volts)	−0.205
$p\varepsilon$	−2.330
$\log f_{O_2}$	−51.285
$\bar{I}$ (molarity)	2.325

Summary of the Aqueous Phase

Component Species	$M^T_{c,aq}$
Na^+	1.00
Ca^{2+}	0.100
K^+	0.038
Mg^{2+}	0.880
UO_2^{2+}	0.16×10^{-5}
Fe^{3+}	0.0005
Cl^-	3.000
CO_3^{2-}	0.00012
SO_4^{2-}	0.001

Summary of the Solid Phase

Mineral	M_m	ϕM_m	Volume Fraction
Muscovite	14.96	2.993	0.4227
Chlorite	0.024	0.0048	0.0011
Uraninite	0.84×10^{-5}	0.17×10^{-5}	0.0000
Kaolinite	0.033	0.007	0.0007
Pyrite	0.200	0.040	0.0010
Quartz	63.87	12.777	0.2897
Graphite	78.75	15.75	0.0848
POROSITY			0.2000

moles/l ($\approx$ 27 ppm) total uranium is assigned, mostly in the form of uranyl-chloride complexes (table 8). This value is about an order of magnitude greater than normal crustal levels (Nash, Granger, and Adams, 1981). However, a bulk solid uranium concentration of 3.0 ppm will produce approx 27 ppm uranium in solution, if all the uranium is leached from the matrix. This starting composition, therefore, defines the premise that all the uranium is transferred from the solid to the aqueous phase at the

TABLE 6

Initial conditions for the sandstone unit

Temperature	100 °C
pH	5.134
E_H (volts)	0.492
$p\varepsilon$	6.642
$\log f_{O_2}$	−22.825
$\bar{I}$ (molarity)	3.997

Summary of the Aqueous Phase

Component Species	$M^T_{c,aq}$
Na^+	1.00
Ca^{2+}	1.502
K^+	0.045
Mg^{2+}	0.477
UO_2^{2+}	0.10×10^{-3}
Fe^{3+}	0.26×10^{-10}
Cl^-	5.000
CO_3^{2-}	0.0001
SO_4^{2-}	0.0015

Summary of the Solid Phase

Mineral	M_m	ϕM_m	Volume Fraction
K-feldspar	4.44	1.11	0.1201
Muscovite	0.518	0.13	0.0183
Anhydrite	0.50	0.125	0.0058
Chlorite	0.0045	0.0011	0.0003
Hematite	1.50	0.375	0.0114
Quartz	104.8	26.2	0.5942
POROSITY			0.2500

beginning of the simulation. It may also be postulated that interbedded volcanics (such as the Nungbalgarri Member in Australia) may provide an elevated source of uranium (Maas, 1989).

Unit 4—Confining unit (table 7), a carbonate-rich shale, in equilibrium with an oxidizing, low-ionic-strength groundwater.

Based on the geometry and parameters shown in figure 7, a single convective cell develops within the sandstone (fig. 8A), with maximum groundwater flow rates of approx 1.1 m/yr. Because of the symmetry assumption, an adjacent counter-clockwise cell would

TABLE 7

Initial conditions for the confining unit

Temperature	50 °C
pH	5.290
E_H (volts)	0.703
$p\varepsilon$	10.971
$\log f_{O_2}$	−14.763
$\bar{I}$ (molarity)	0.197

Summary of the Aqueous Phase

Component Species	$M^T_{c,aq}$
Na^+	0.10
Ca^{2+}	0.028
K^+	0.022
Mg^{2+}	0.0026
UO_2^{2+}	0.10×10^{-4}
Fe^{3+}	0.73×10^{-14}
Cl^-	0.10
CO_3^{2-}	0.396
SO_4^{2-}	0.015

Summary of the Solid Phase

Mineral	M_m	ϕM_m	Volume Fraction
Muscovite	0.078	0.008	0.0011
Calcite	133.1	13.3	0.4914
Dolomite	2.00	0.20	0.0129
Anhydrite	0.515	0.052	0.0024
Kaolinite	29.9	2.99	0.2967
Hematite	0.10	0.010	0.0003
Quartz	42.0	4.20	0.0952
POROSITY			0.1000

develop to the left, but only a single cell is simulated to reduce the computational effort. Flow is clockwise, with a small component of flow entering the basement rocks and focused through the graphite unit and back into the basin (fig. 8B). Temperatures are modified by advection of thermal energy (fig. 8C), such that temperatures are higher at the unconformity above the graphite (>180°C; fig. 8D) than at the unconformity at the other side (<140°C) where groundwater flow is downward.

TABLE 8

Predominant aqueous uranium species initially present in the sandstone unit

Species	Molarity*	Percent of Total†
UO_2Cl^+	4.6×10^{-5}	46
$UO_2Cl_2^0$	4.28×10^{-5}	42.8
UO_2^{2+}	9.8×10^{-6}	9.8
$UO_2SO_4^0$	6.33×10^{-7}	0.633
$UO_2CO_3^0$	6.2×10^{-7}	0.62
$UO_2HCO_3^+$	1.9×10^{-8}	0.02

* At 100°C

† Total aqueous uranium = 10^{-4} moles/l (table 6)

Based on these starting conditions (including flow geometry, groundwater velocities, and temperatures) uraninite is precipitated above the unconformity forming a significant ore body within 500,000 yrs (fig. 9). Although the maximum grade is small (<0.1 wt percent), due to the assumption of linear interpolation between nodes, integration of mass concentrations over the area of maximum precipitation produces 143,000 tons of uraninite, assuming the deposit is symmetric about the left boundary, and is 1 km in length. This predicted tonnage compares favorably with measurements on actual deposits (table 1). Once this configuration has been achieved, continued deposition of uraninite occurs within the same region.

The immediate conclusion drawn here is that free convection within the basal sandstone is capable of producing significant quantities of uranium ore in less than 1 Ma. Moderate starting uranium concentrations within the sandstone are required to produce this result (<30 ppm), but smaller concentrations would still produce significant quantities of uraninite, given sufficient time. Furthermore, transport as uranyl-chloride complexes is clearly reasonable, given the large concentration of chloride in the ore-forming fluid (table 8). Uraninite is precipitated near the unconformity and within a very small area (400 by 100 m), replicating in general the observed geometry of the ore deposits. In this case, uraninite is precipitated as oxidizing, uranium-bearing groundwater encounters reducing conditions near the unconformity. A stable redox interface develops (fig. 10) where basement fluids re-enter the basin through the permeable (fractured) graphite.

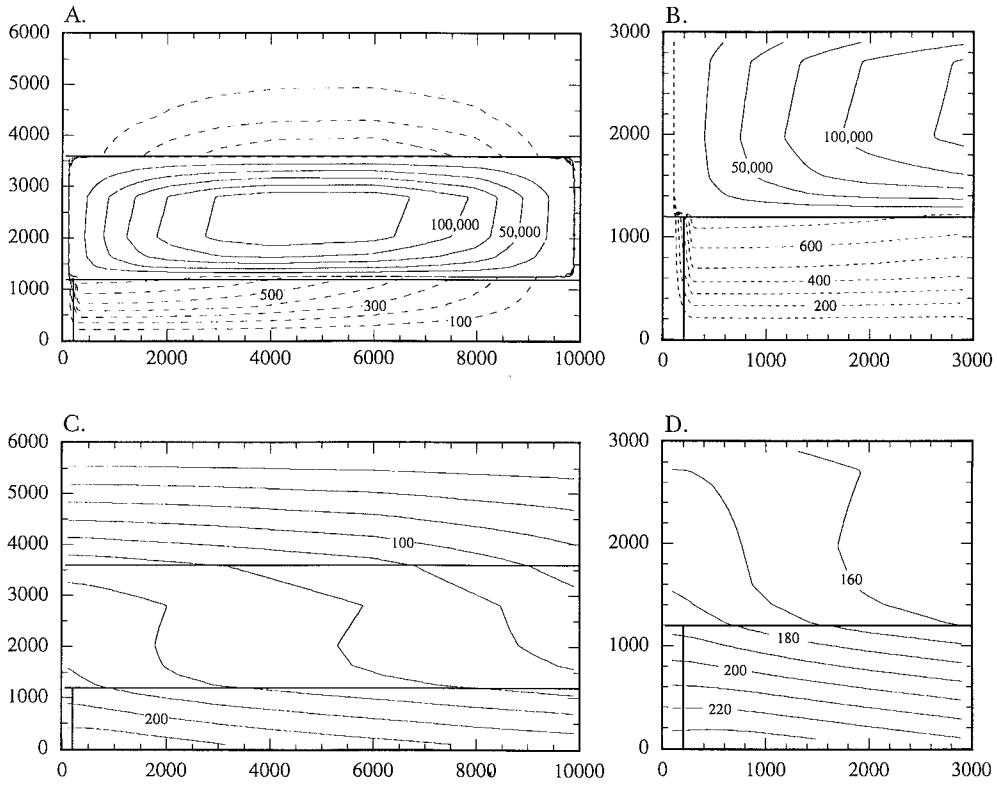

Fig. 8. Steady state stream function (A) and temperature (C) with expanded views (B, D). Contour interval for stream function is 100 kg/m yr (dotted lines) or 25,000 kg/m yr (solid lines). Contour interval for temperature is 20°C (C) or 10°C (D). Solid lines indicate boundaries of hydrostratigraphic units. Axes units are meters.

Several simulations were conducted that did not produce the desired result, that is, precipitation of significant quantities of uraninite near the unconformity above the graphite. We may briefly and qualitatively outline the reasons for failure in these cases. When basement rocks contain greater quantities of methane (more reducing), uraninite tends to precipitate all along the unconformity, where dispersion causes basin fluids to interact with the basement. On the other hand, high concentrations of carbonate in the basement (more oxidizing, $M^T_{CO_3^{2-},aq} > 0.10$) produced carbonates as the major gangue minerals, a result not typically associated with unconformity-type uranium deposits (see table 1). This places some constraints on the starting composition of the basement rocks and fluid. The geometry of the flow system plays an important role

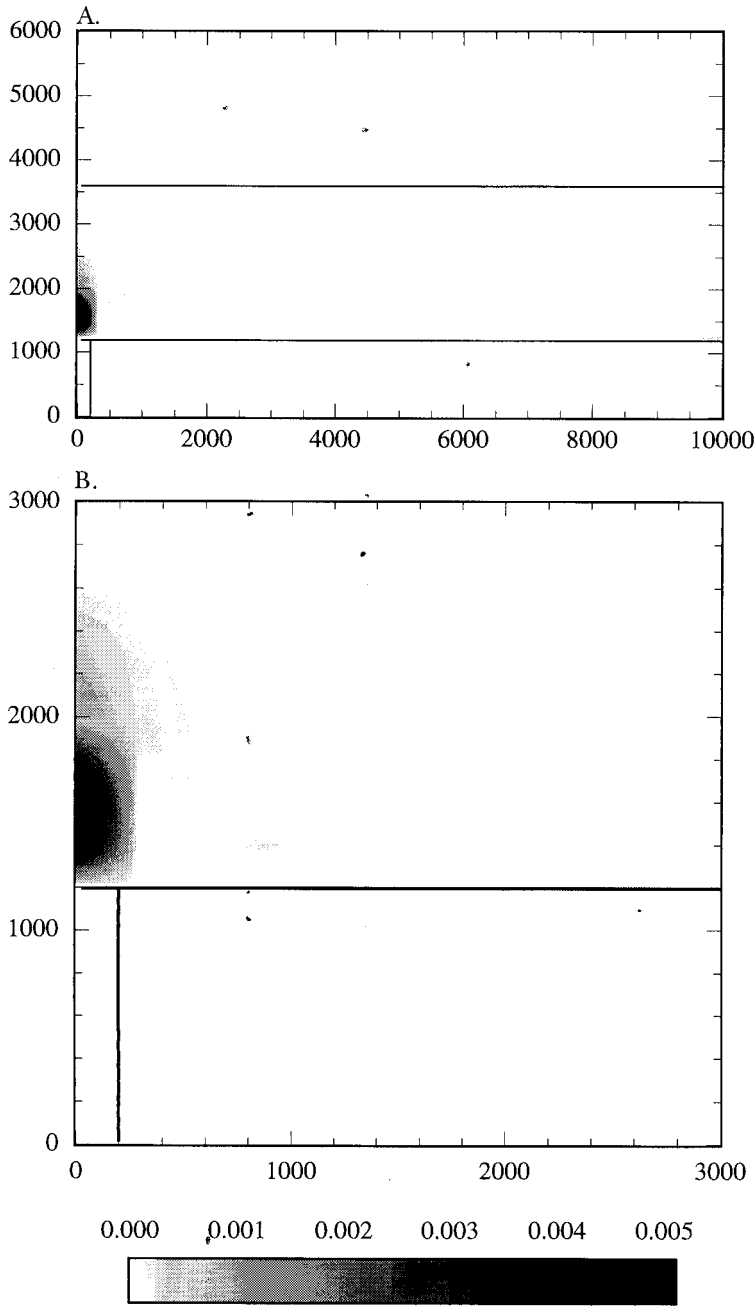

Fig. 9. Concentration of uraninite after 500,000 yrs (A) and expanded view (B). Concentrations are expressed as moles/liter bulk porous medium. Solid lines indicate boundaries of hydrostratigraphic units. Axes units are meters.

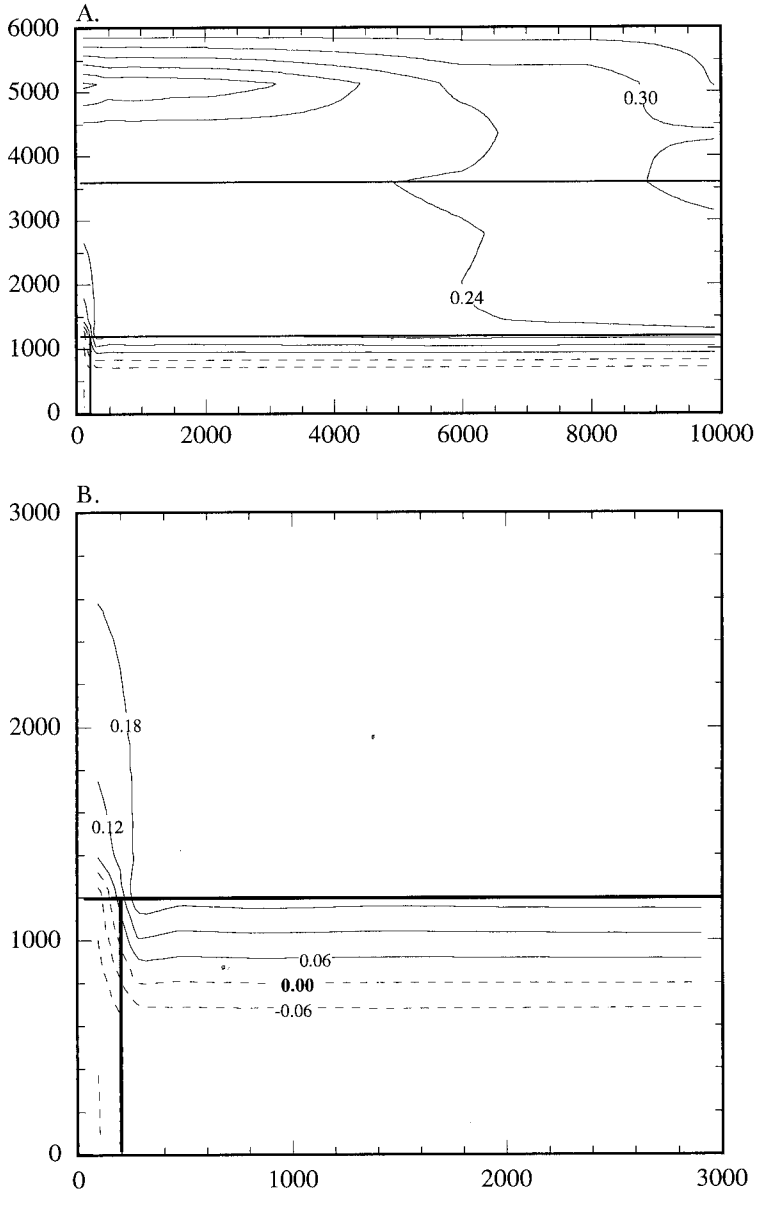

Fig. 10. E_H at 500,000 yrs (A) and expanded view (B). Contour interval is 0.06 volts, and dotted contours indicate negative values. Solid lines indicate boundaries of hydrostratigraphic units. Axes units are meters.

in determining where uraninite precipitates. When the graphite unit is assumed to have a permeability matching the basement (no contrast) the result is that flowlines penetrating the basement (see fig. 8A) re-enter the sandstone unit along half the unconformity, rather than being focused at the graphite unit. Uraninite precipitates along the unconformity wherever upward flow across the unconformity transports reductant (methane) into the basin, producing a low grade deposit 5 km wide. Focusing of groundwater flow across the unconformity by fracturing and faulting of graphitic basement rocks is therefore essential to the development of large unconformity-type uranium deposits.

According to the diagenetic-hydrothermal model of unconformity-type uranium ore formation, diagenetic changes accompany ore formation, producing alteration halos observed to be associated with these ores. Minerals most often associated with these alteration halos include muscovite (sericite), chlorite, quartz, hematite, and pyrite (table 1). After 500,000 yrs, muscovite precipitation has formed a halo surrounding the uranium deposit (fig. 11) which persists through at least 1 Ma of mineralization. This halo initially develops as a narrow band along the unconformity due to mass transport (especially dispersion) across the boundary. Alteration then migrates to form a halo surrounding the deposit. Chlorite precipitation occurs in a similar manner (fig. 12), forming a halo by 500,000 yrs which persists for longer periods of time. Note, however, that significant chlorite precipitation occurs in a small zone just below the deposit (fig. 12C), unlike muscovite which precipitates both within the ore and around it (fig. 11C). The major gangue mineral at the unconformity is chlorite.

Hematite precipitation follows a trend similar to chlorite (fig. 13), although hematite dissolves just below the zone of uraninite and hematite precipitation at the unconformity (fig. 14A). In this area, and throughout the basement, Fe (hematite) is reduced to form pyrite (fig. 14B). Muscovite (fig. 11) and quartz (fig. 15A) form at the expense of K-feldspar, which is removed from the zone of alteration within the sandstone (fig. 15B). In addition, K-feldspar precipitates at the unconformity just below the ore, within the basement rocks, and within the sandstone outside the major alteration halo; quartz dissolution mimics this pattern (results not shown).

We can examine mineralogical changes along a vertical transect through this alteration halo, in order to examine major reactions and fluxes of mass which occur. Taking a line through $X = 0$, the left boundary, changes in the major aluminosilicates (fig. 16) indicate that a balanced reaction occurring in the altered sandstone may be written:

$$1.04\text{K-feldspar} + 0.371\text{Mg}^{2+} + 0.206\text{SiO}_2^0 + 0.011\text{Al}^{3+} + 0.62\text{H}_2\text{O}$$
$$\rightarrow 0.3\text{Muscovite} + 2.2\text{Quartz} + 0.074\text{Chlorite} + 0.74\text{K}^+ + 0.04\text{H}^+$$

which indicates that magnesium and silica are added to and potassium removed from the altered zone. At the unconformity, a balanced reaction

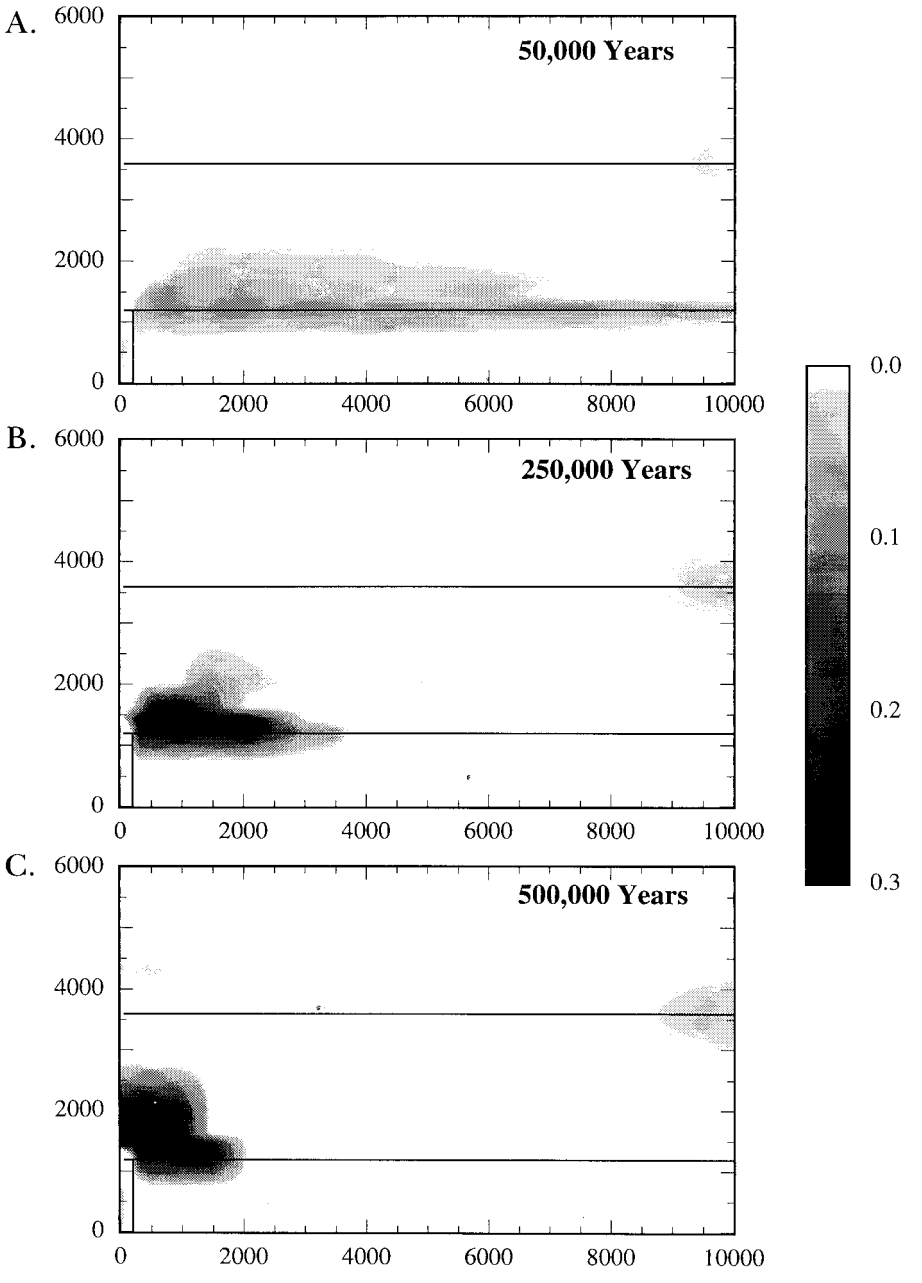

Fig. 11. Muscovite precipitated after (A) 50,000, (B) 250,000, and (C) 500,000 yrs. Concentrations are expressed as moles/liter bulk porous medium. Solid lines indicate boundaries of hydrostratigraphic units. Axes units are meters.

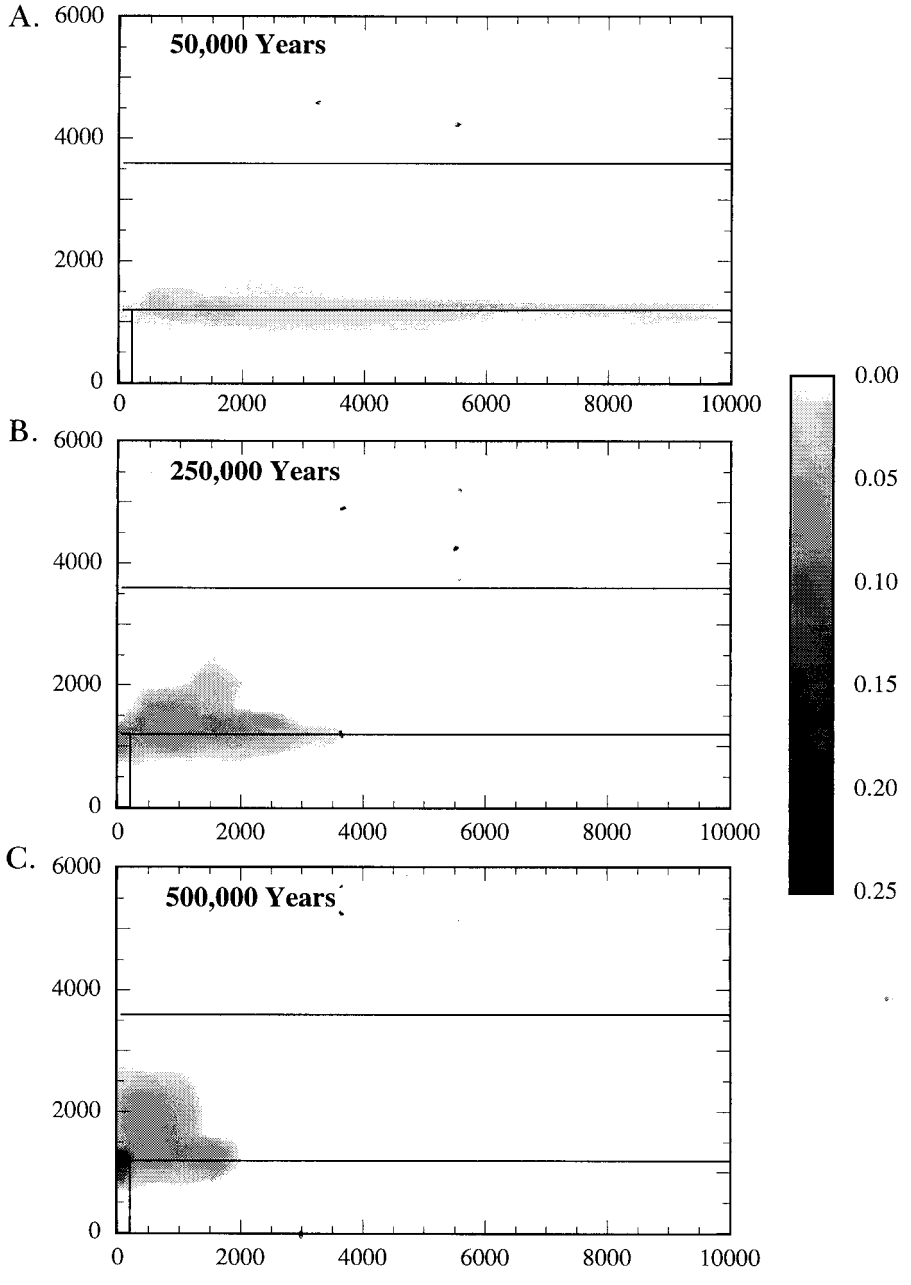

Fig. 12. Chlorite precipitated after (A) 50,000, (B) 250,000, and (C) 500,000 yrs. Concentrations are expressed as moles/liter bulk porous medium. Solid lines indicate boundaries of hydrostratigraphic units. Axes units are meters.

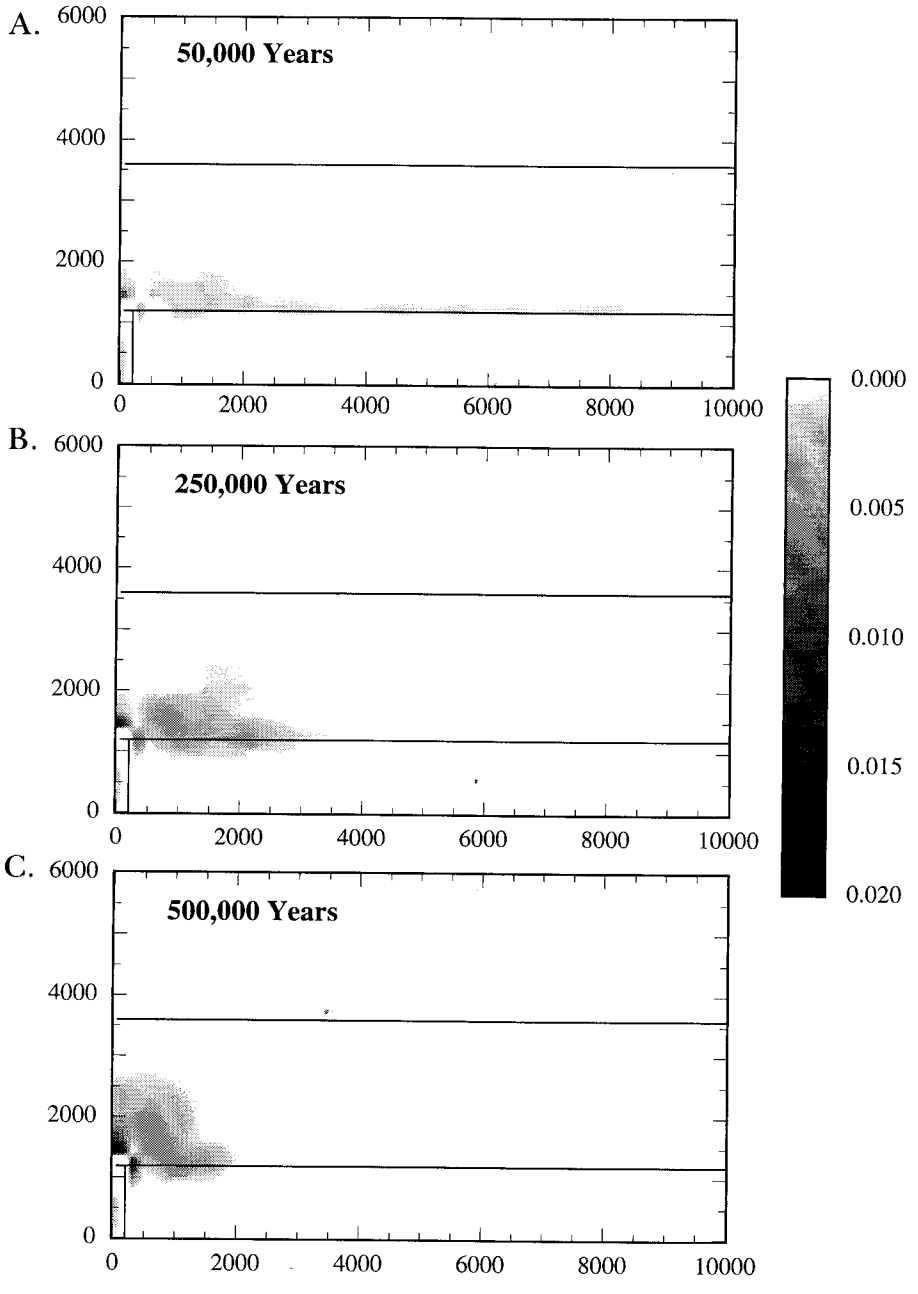

Fig. 13. Hematite precipitated after (A) 50,000, (B) 250,000, and (C) 500,000 yrs. Concentrations are expressed as moles/liter bulk porous medium. Solid lines indicate boundaries of hydrostratigraphic units. Axes units are meters.

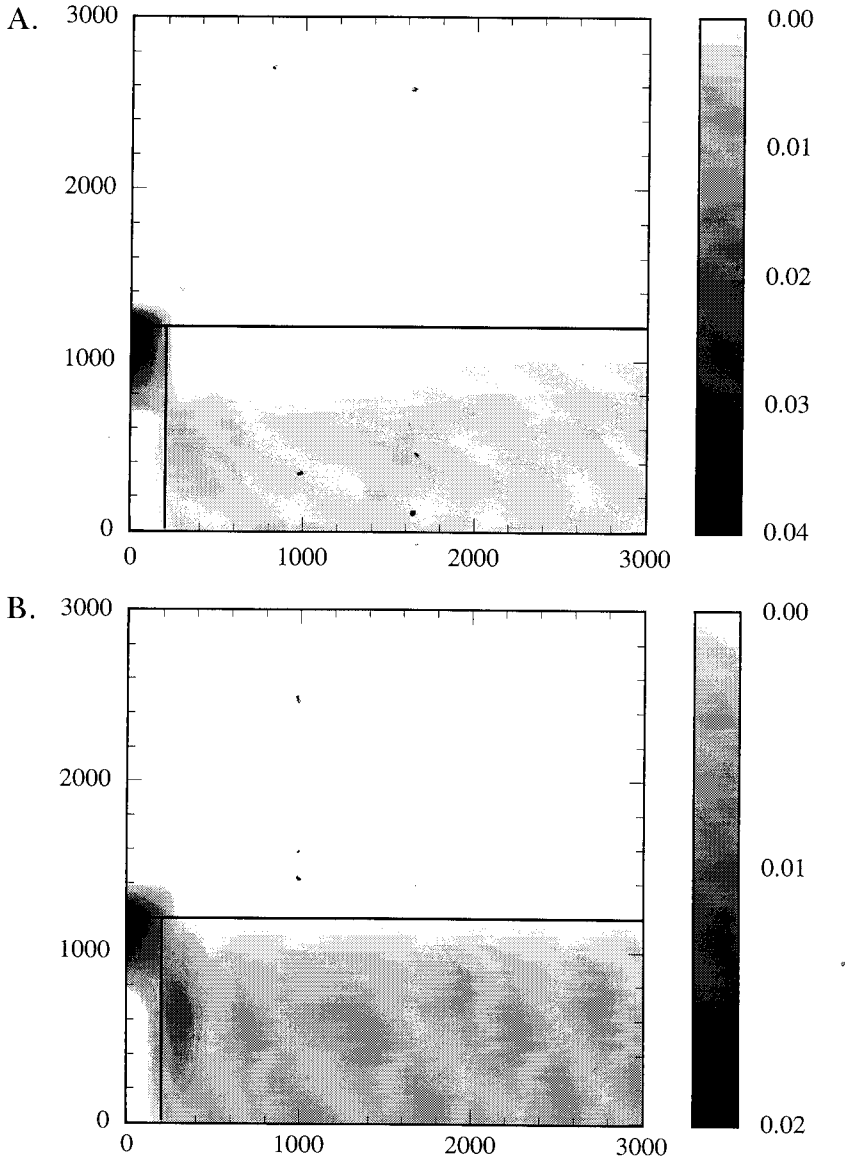

Fig. 14. Expanded view of hematite dissolved (A) and pyrite precipitated (B) after 500,000 yrs. Concentrations are expressed as moles/liter bulk porous medium dissolved (A) and precipitated (B). Solid lines indicate boundaries of hydrostratigraphic units. Axes units are meters.

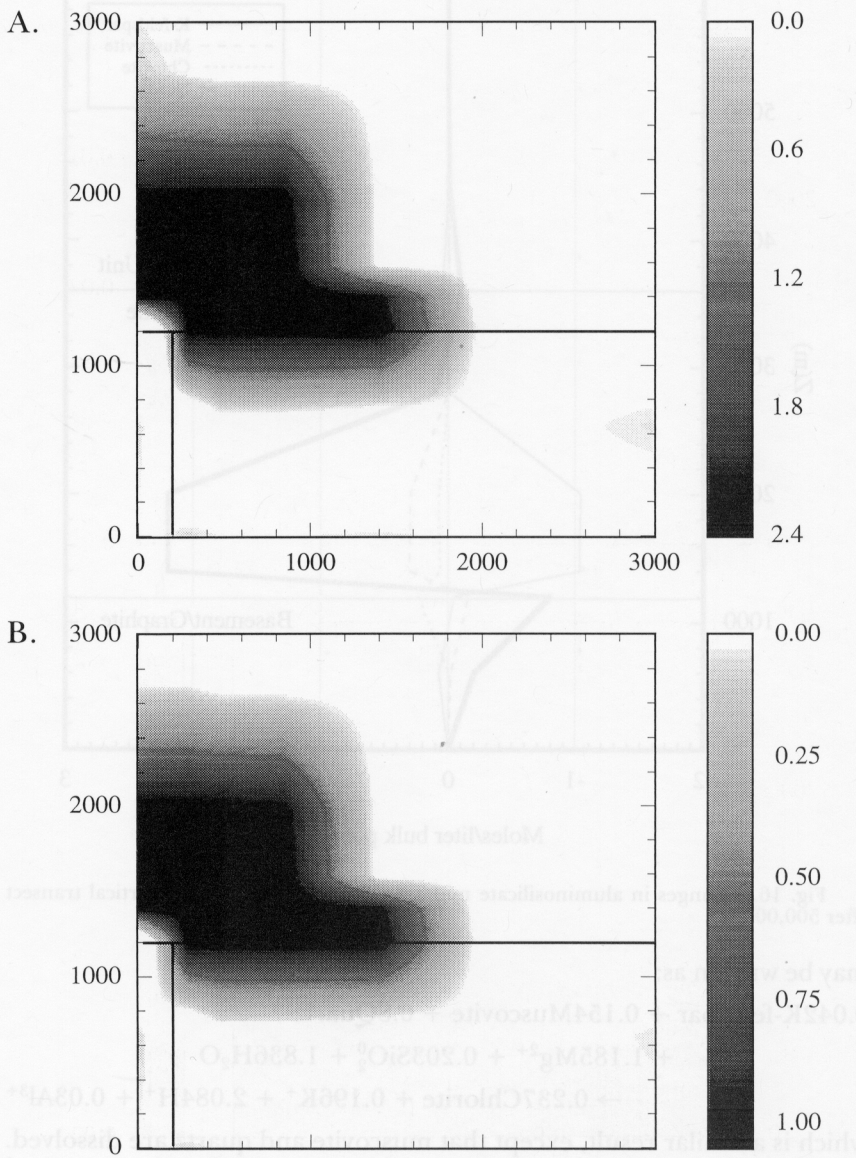

Fig. 15. Expanded view of quartz precipitated (A) and K-feldspar dissolved (B) after 500,000 yrs. Concentrations are expressed as moles/liter bulk porous medium precipitated (A) and dissolved (B). Solid lines indicate boundaries of hydrostratigraphic units. Axes units are meters.

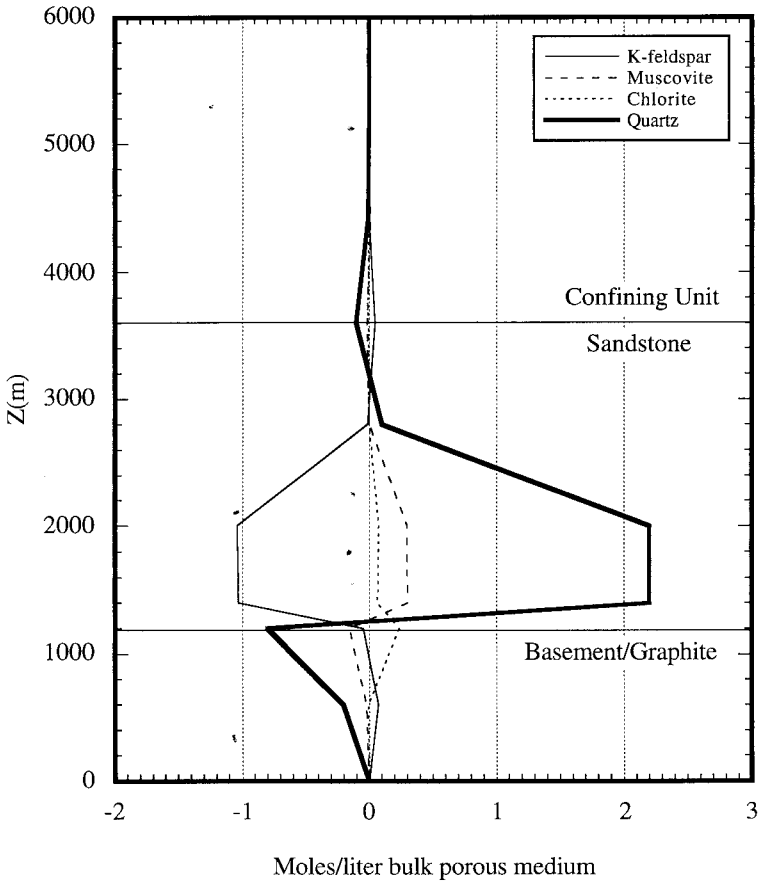

Fig. 16. Changes in aluminosilicate mineral concentrations along a vertical transect after 500,000 yrs.

may be written as:

$$0.042\text{K-feldspar} + 0.154\text{Muscovite} + 0.8\text{Quartz} + 1.185\text{Mg}^{2+} + 0.203\text{SiO}_2^0 + 1.836\text{H}_2\text{O} \rightarrow 0.237\text{Chlorite} + 0.196\text{K}^+ + 2.084\text{H}^+ + 0.03\text{Al}^{3+}$$

which is a similar result, except that muscovite and quartz are dissolved. This reaction is similar to that proposed by Nutt (1989), who suggested that a drop in pH accompanying chloritization could promote uraninite precipitation by de-stabilizing uranyl-carbonate complexes. Chlorite precipitation at the unconformity is favored by the large amount of magnesium in solution which is transported upward from the graphite unit (table 5) and by the fact that the chlorite stability field increases with temperature (fig. 17).

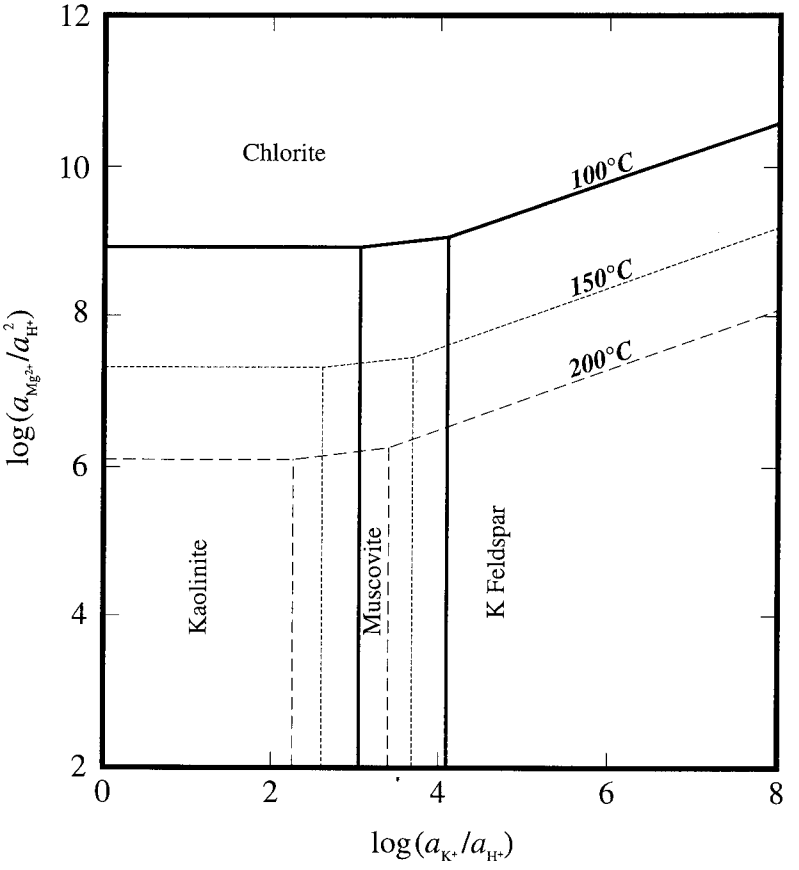

Fig. 17. Phase diagram for the system H_2O–Al_2O_3–K_2O–MgO–SiO_2. The activity of H_2O is assumed to be 1, and quartz saturation is assumed.

Hematite precipitates within and around the ore zone, just above the unconformity and well up into the sandstone (fig. 18). Iron oxidation (forming hematite) is accompanied by uranium reduction, precipitating uraninite within the zone of hematite formation. At and below the unconformity, pyrite forms due to the strong reducing capability of the graphite-rich rock and a slightly lower pH (figs. 19 and 20). Reducing conditions are found near and below the unconformity, a condition that persists for at least 500,000 yrs (fig. 21).

Changes in porosity (ϕ) accompany these mineralogical changes, with porosity increasing above the unconformity, and decreasing by more than 0.6 percent at the unconformity (fig. 22). Using the equation of Walsh (1983), a 0.6 percent decrease in ϕ would produce a 25 percent reduction in permeability. Combined with muscovite and chlorite precipi-

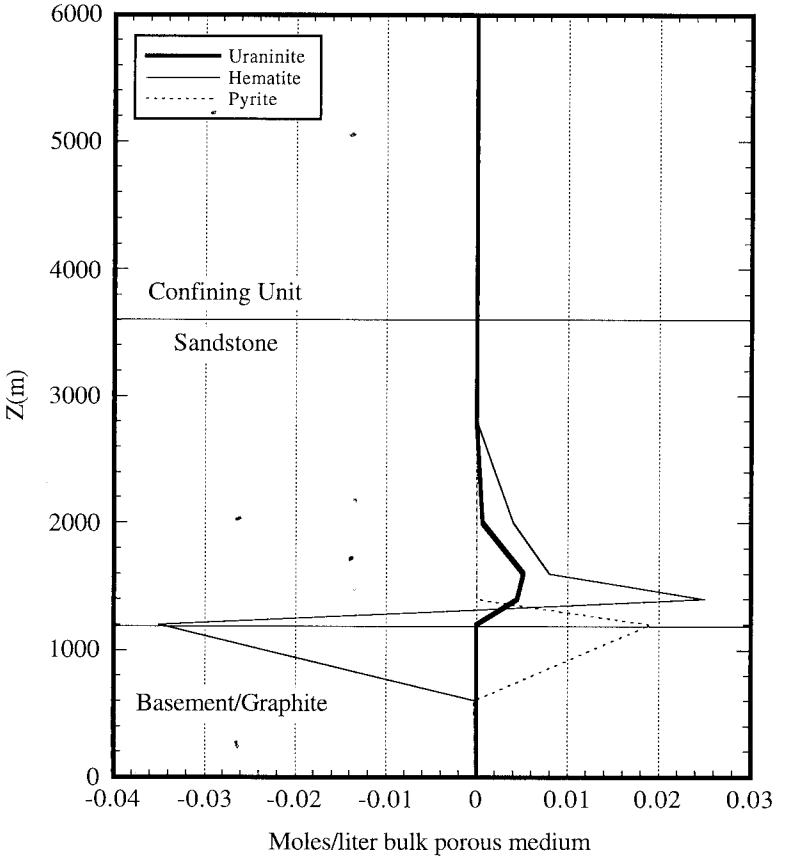

Fig. 18. Changes in Fe-mineral concentrations and uraninite along a vertical transect after 500,000 yrs.

tation, the region of increased porosity within the sandstone resembles the "friable" zone associated with the Cigar Lake and Midwest deposits.

We have considered mineralogical changes associated with uraninite precipitation in the vicinity of the unconformity and recognized a trend associated with unconformity-type uranium mineralization: a narrow ore zone surrounded by concentric zones of hydrothermal alteration, predominantly chlorite, muscovite, and hematite. In addition, the prediction of pyrite precipitation within the basement rocks beneath the ore zone, as has been observed at Cigar Lake, lends some confidence to the model. Temporal changes in mineralogy at a single point in the flow field resemble the results of closed system reaction path calculations, although disequilibrium due to physical mass transport rather than initial conditions drives these changes. We can construct a calculated paragenetic

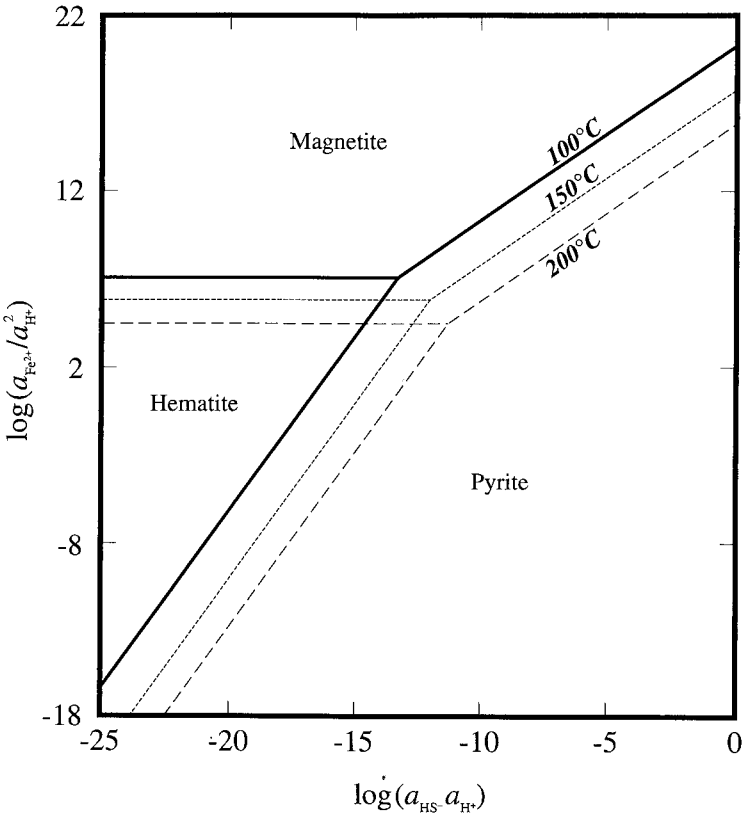

Fig. 19. Phase diagram for the system H_2O–FeO–H_2S. The activity of H_2O is assumed to be 1.

sequence for the observed zones of alteration, based on these temporal changes (fig. 23). In the altered basement rocks, muscovite is totally removed after 150,000 yrs, while chlorite precipitates steadily. Pyrite forms almost immediately, and small amounts of dolomite precipitate after 200,000 yrs. The compositional boundary represented by the unconformity results in relatively rapid mineralogical changes. Within the zone of ore formation, nearly 300,000 yrs is required to reach a relatively stable mineral assemblage, after which time uraninite and hematite precipitation are the primary reactions taking place. Between 250,000 and 300,000 yrs are required for K-feldspar to be replaced by chlorite and additional muscovite. Within the altered sandstone, 400,000 yrs are required for this change. We may conclude that while uraninite precipitation proceeds immediately and solid uranium concentrations increase monotonically within the ore zone, the alteration halo itself requires up to 500,000 yrs to form, with regions closest to the unconfor-

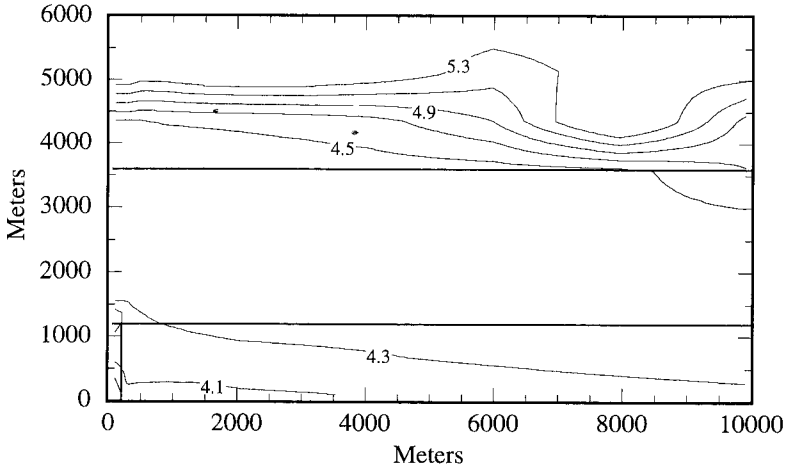

Fig. 20. pH at 500,000 yrs. Solid lines indicate boundaries of hydrostratigraphic units.

mity experiencing the most rapid development of the major gangue minerals (muscovite, chlorite, quartz, hematite).

From these calculations, we may conclude that free convection within a sedimentary basin of a uranium-bearing chloride brine, under moderately oxidizing conditions, may precipitate ore-grade quantities of uraninite in the vicinity of the unconformity between basin sandstones and basement graphite schists. In these calculations, we have assumed that upwelling is focused at the graphite zone. A small component of flow within the basement brings reductant up the permeable graphite zone, which produces a stationary redox front at the unconformity. The resultant hydrothermal alteration halo closely resembles many aspects of unconformity-type uranium ores.

II. *Free convection with lateral flow at the graphite unit.*—Another hydrochemical scenario might be envisioned in which vertical flow is not centered or focused at the graphite unit. As was shown in part 1, basin geometry and permeability are the key factors influencing free convection within the sandstone. Higher thermal conductivities associated with the graphite-bearing rocks generally were not found to influence the position of individual cells. Using the same boundary conditions as previously, but with a grid that has the graphite unit at its center (fig. 24), the streamline pattern is slightly different (although still clockwise), and temperatures are lower in the vicinity of the unconformity above the graphite (fig. 25). Initial conditions are the same as the first simulation (tables 4-7). The results indicate that after 250,000 yrs, a diffuse ore body has formed above the graphite (fig. 26A). However, muscovite and chlorite precipitation patterns do not resemble the alteration halos associated with the deposits (figs. 26B and C). Much of the chlorite and

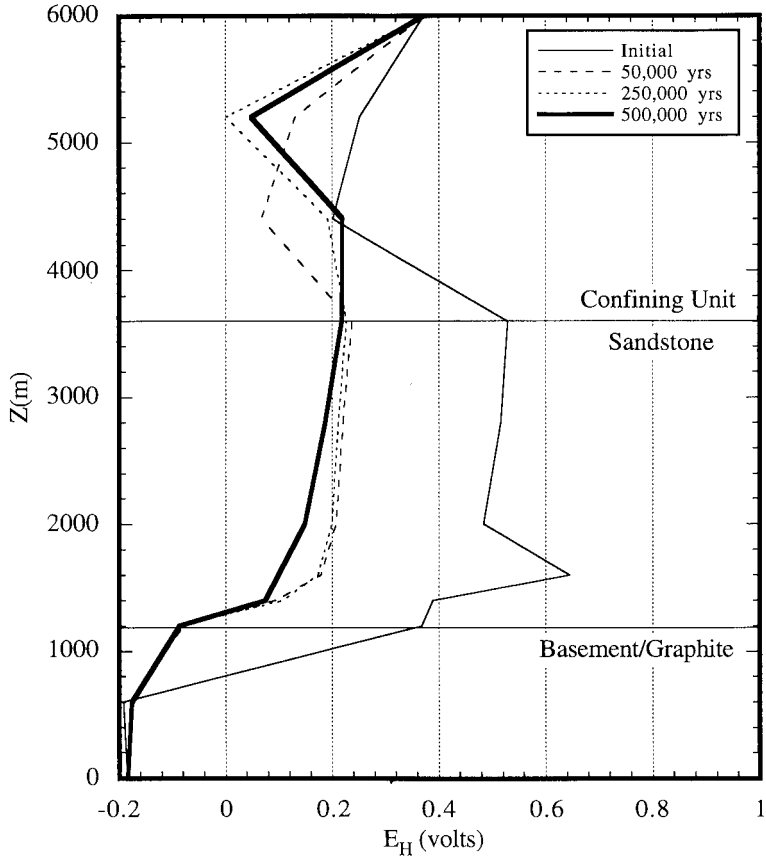

Fig. 21. E_H as a function of time along a vertical transect.

muscovite precipitation still occurs at the left, where the upwelling limb of the convection cell transports mass through higher temperatures and across isotherms.

III. *Gravity-driven flow.*—In part 1, topography was investigated as a possible driving force for groundwater flow in the Proterozoic Athabasca and McArthur Basins. If sufficient topographic relief existed at the time of ore formation, free convection may have been overwhelmed by lateral groundwater flow or "forced" convection. As a result, streamlines would be nearly horizontal within the sandstone (fig. 27A), and the temperature gradient would be due to conduction alone (fig. 27B), although on a basin scale lateral flow may raise temperatures at the discharge end of the basin (see discussion in part 1). Maximum flow velocities are approx 0.85 m/yr, based on a water table slope of 0.001 m/m. We can simulate the

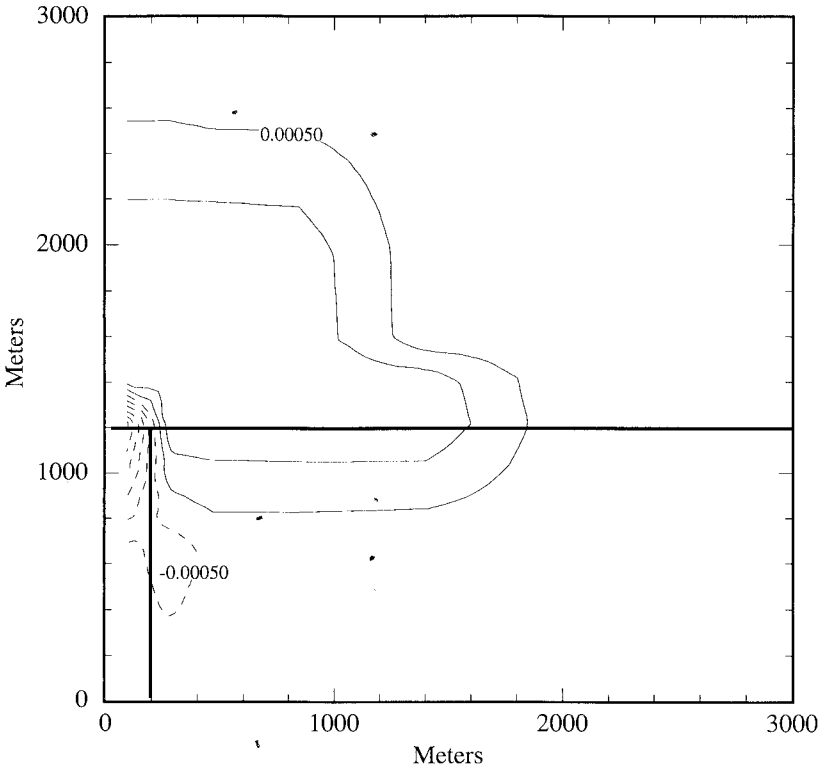

Fig. 22. Expanded view of porosity changes after 500,000 yrs. Dotted contour lines indicate regions of net precipitation or porosity loss, and solid contour lines indicate areas of net porosity gain. Changes are expressed as volume fractions, and solid lines indicates boundaries of hydrostratigraphic units.

effect of this flow configuration on the formation of an ore deposit, assuming constant concentrations at the left (inflow) boundary.

Uraninite precipitates near the unconformity, although the pattern is more diffuse (fig. 28A), as was the case for a centered graphite unit in a free convection system. However, some uraninite does precipitate within the basement rocks, a result that differs from the first free convection case. Several unconformity-type uranium deposits, especially the Australian deposits, are hosted partially or completely by metamorphic basement rocks, an observation that appears to be accounted for by this hydrologic system. However, no alteration halo surrounding the deposit develops in this scenario. Rather, muscovite (fig. 28B) and chlorite (fig. 28C) precipitation is limited to the basement rocks along the length of the unconformity. This pattern of alteration is the result of mass transport (predominantly dispersion) across the compositional boundary. From

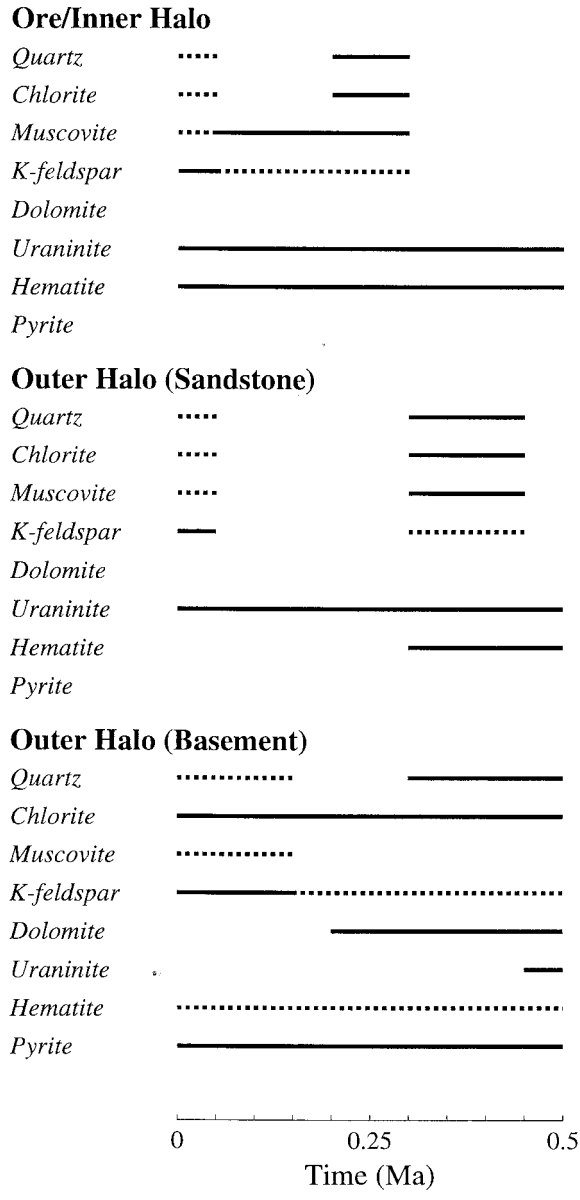

Fig. 23. Calculated paragenetic sequence. Solid lines indicate precipitation and dashed lines indicate dissolution.

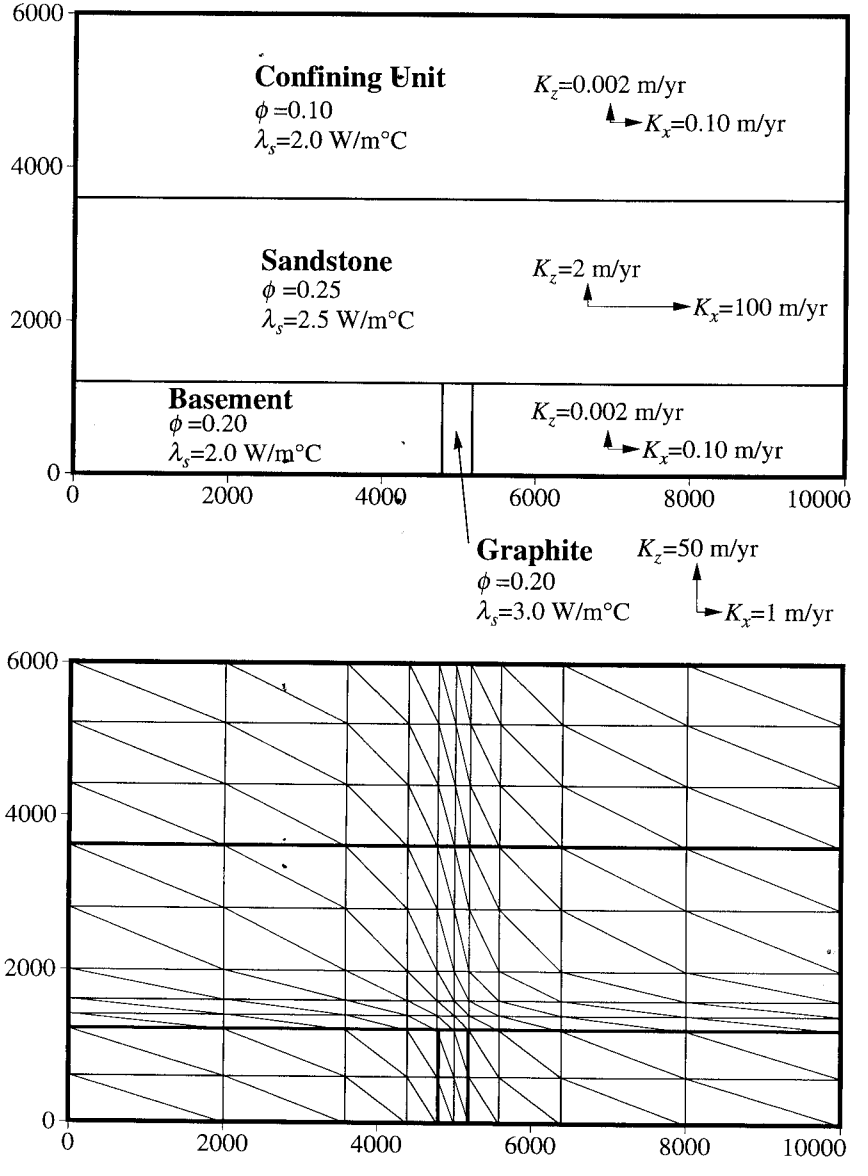

Fig. 24. Hydrostratigraphy and finite element mesh for the case where graphite is at the center. Axes units are meters.

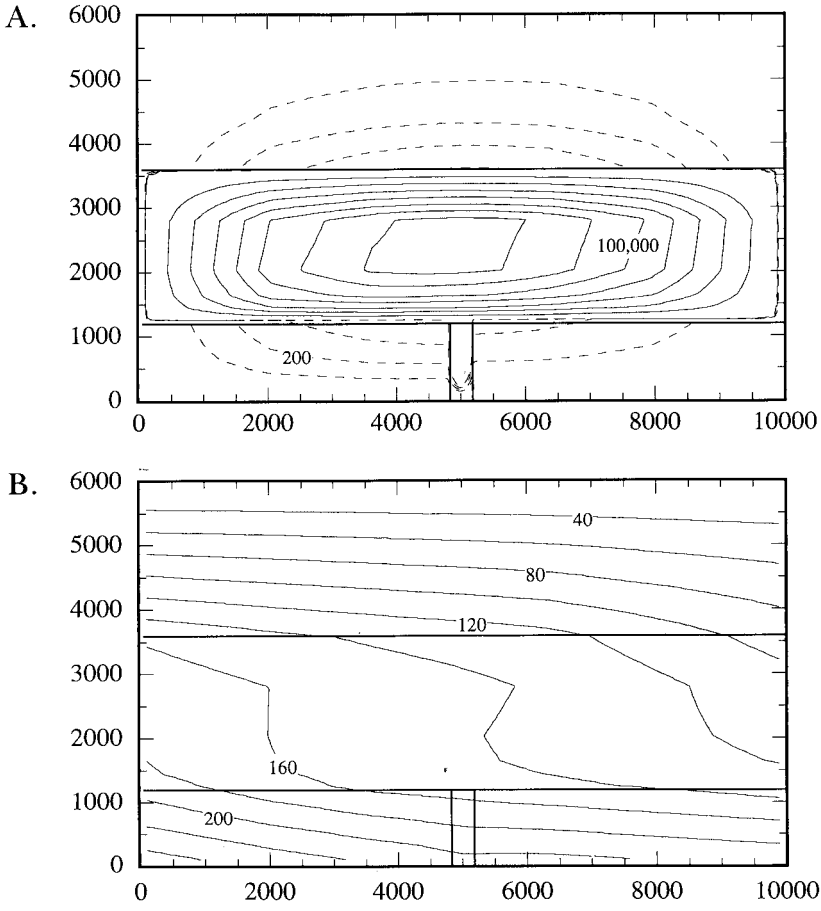

Fig. 25. Steady state stream function (A) and temperature (B) for the case of a centered graphite unit. Contour interval for stream function is 100 kg/m yr (dotted lines) or 20,000 kg/m yr (solid lines). Contour interval for temperature is 20°C. Solid lines indicate boundaries of hydrostratigraphic units. Axes units are meters.

this analysis we may conclude that the hydrologic flow field and resulting temperature pattern play a prominent role in the formation of an ore deposit and associated alteration. Specifically, a free convection system, unlike a topographically-driven flow system, provides: (1) for focusing of flow at the unconformity, limiting the extent of alteration, (2) for locally elevated temperatures, promoting certain alteration patterns, and (3) for advective mass transport across the basin-basement boundary, supplying Mg^{2+} and the reductant.

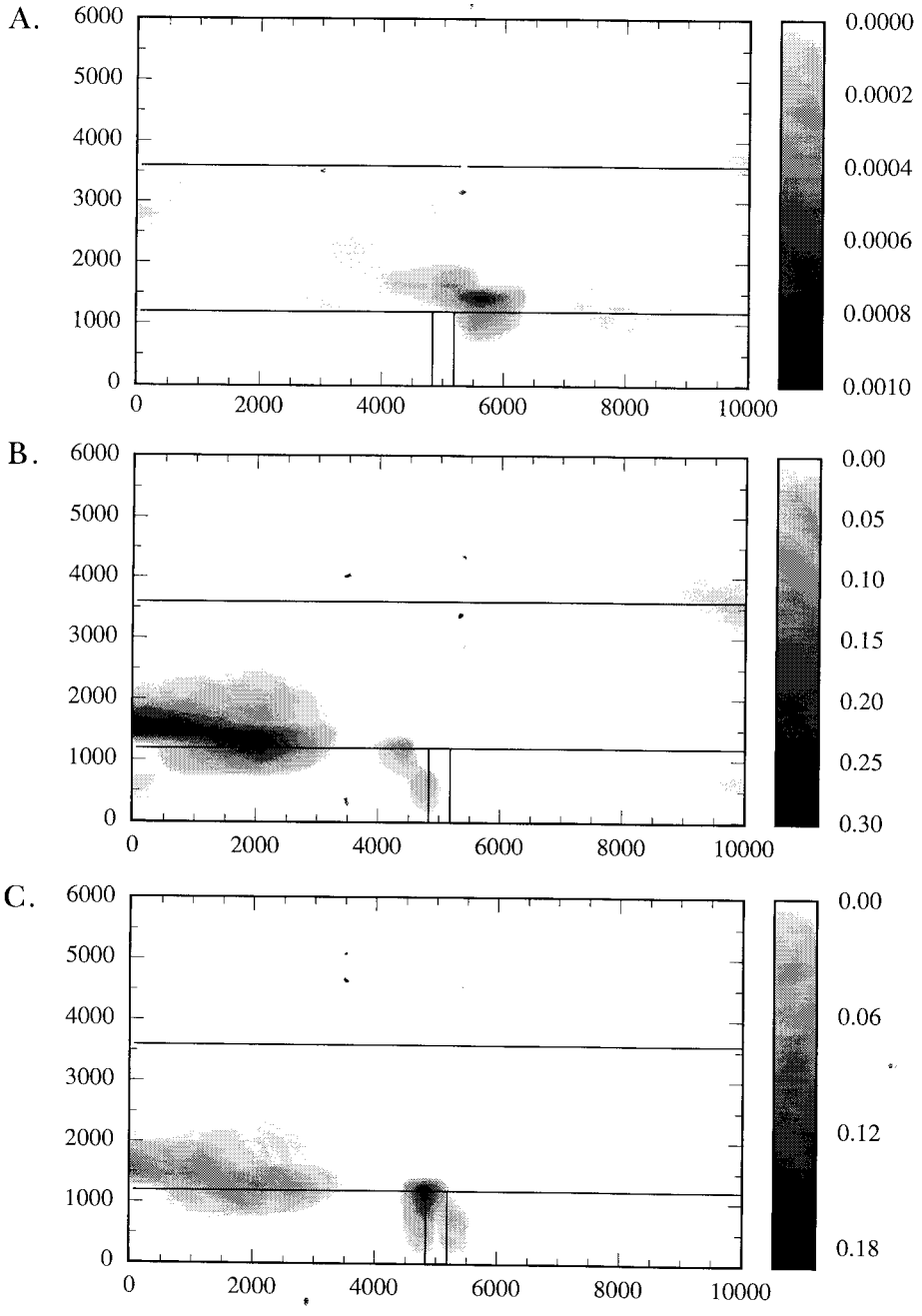

Fig. 26. Uraninite concentration (A), muscovite precipitated (B), and chlorite precipitated (C) after 250,000 yrs for the case of a centered graphite unit. Units are moles/liter bulk porous medium. Solid lines indicate boundaries of hydrostratigraphic units. Axes units are meters.

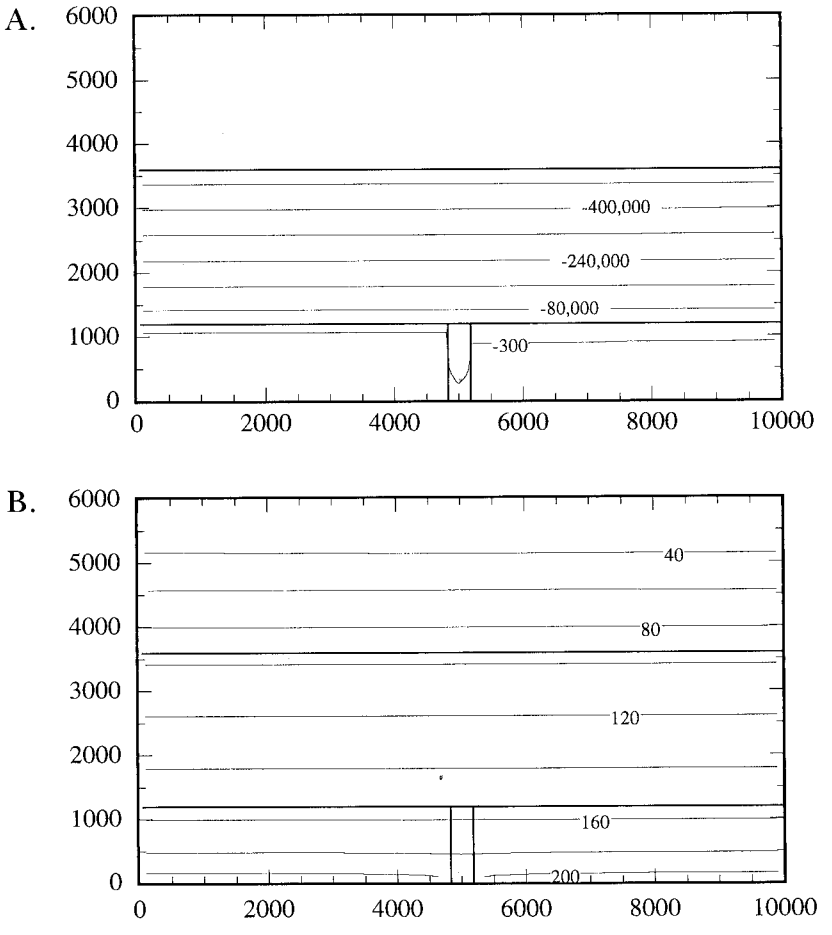

Fig. 27. Steady state stream function (A) and temperature (B) for the case of a gravity-driven flow system. Direction of flow is from left to right. Contour interval for stream function is 80,000 kg/m yr, although a single contour line at 300 kg/m yr is added. Contour interval for temperature is 20°C. Solid lines indicate boundaries of hydrostratigraphic units. Axes units are meters.

SUMMARY AND CONCLUSIONS

According to the diagenetic-hydrothermal model for the formation of unconformity-type uranium deposits, oxidizing, uranium-bearing meteoric waters move downward through the basin sands, precipitating uraninite at a stable redox interface in the vicinity of the unconformity. The uranium is thought to derive from the thick sandstone sequences found within the Middle Proterozoic Athabasca and McArthur Basins and to have been transported as soluble uranyl-carbonate complexes (McLennan and Taylor, 1979). Reducing conditions are conjectured to

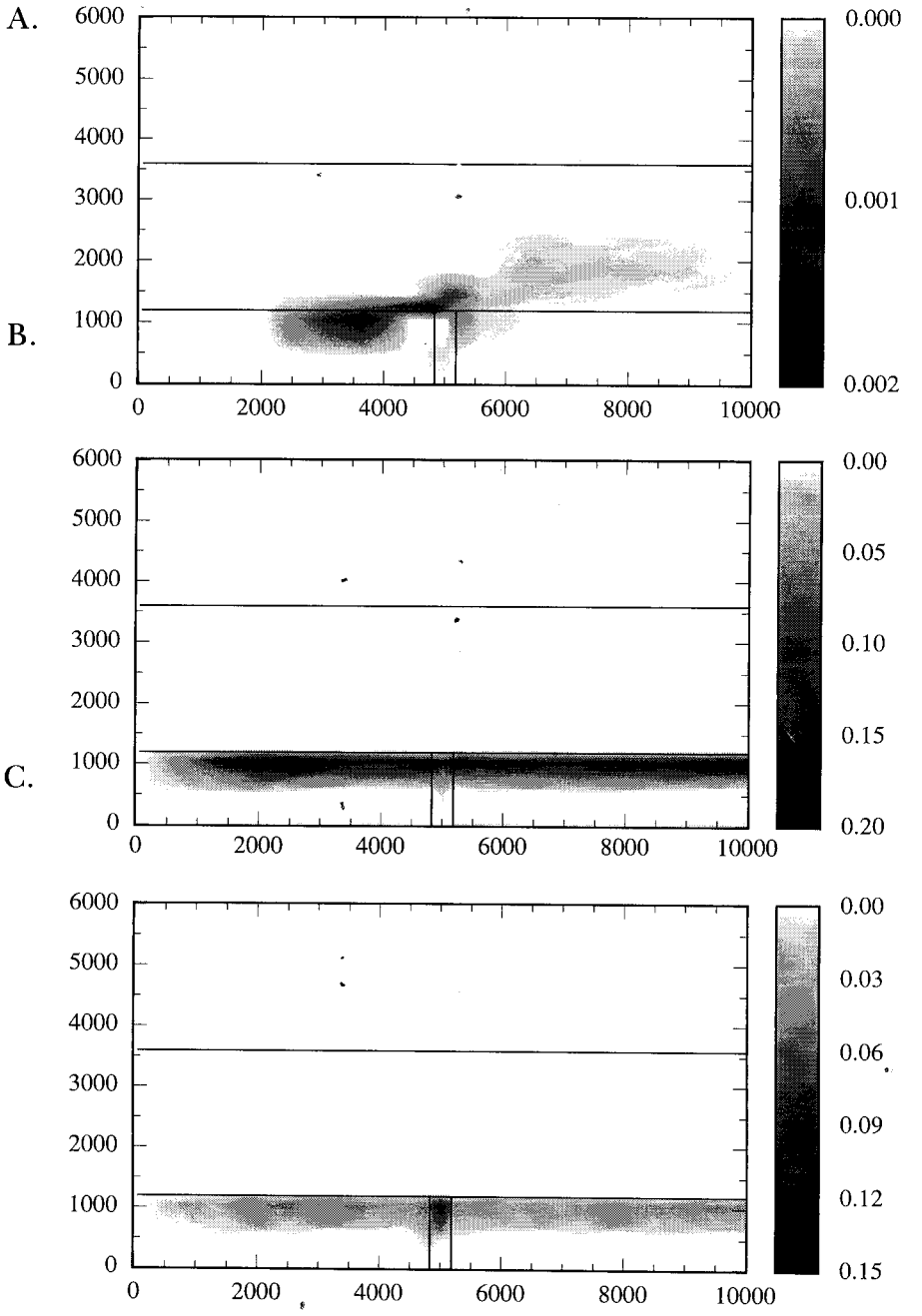

Fig. 28. Uraninite concentration (A), muscovite precipitated (B), and chlorite precipitated (C) after 200,000 yrs for the case of a gravity-driven flow system. Units are moles/liter bulk porous medium. Solid lines indicate boundaries of hydrostratigraphic units. Axes units are meters.

result from hydrothermal alteration of graphite, producing methane that moves upward through faulted basement structures associated with the graphite schist. In addition, these faulted basement structures are considered crucial in localizing uranium mineralization.

Strong hydrothermal alteration, including sericitization and chloritization of the host lithologies, is intimately related to the formation of these deposits. Virtually all the deposits demonstrate similar paragenetic patterns, which involve (in addition to chlorite and mica) quartz precipitation and dissolution, pyrite formation and possibly several episodes of hematite precipitation and dissolution. Studies have examined these paragenetic patterns (Gustafson and Curtis, 1983; Hoeve and Quirt, 1984; Wilde and Wall, 1987; Percival, 1989), which have indicated that mineralization is accompanied by introduction of H_2O and magnesium and leaching of silica, potassium, and ferrous iron (Hoeve and Sibbald, 1978). Some of these deposits indicate redistribution of silica, rather than leaching, as evidenced by the quartz cap at Cigar Lake (Bruneton, 1987).

The purpose of this study was to quantify the ore-forming and alteration process, through application of a coupled two-dimensional model of groundwater flow, heat transport, and reactive multicomponent solute transport. This numerical model enables the calculation of the spatial distribution of minerals and how that distribution changes through time. Several simplifying assumptions were made: (1) local equilibrium; (2) a sandstone source for uranium, such that initial conditions included an evenly distributed uranium concentration within the sandstone; and (3) steady state groundwater flow, that is, changes in porosity and permeability as a function of time were not allowed to alter the flow pattern. Furthermore, a simplified geometry was chosen, consisting of a 2.4 km sandstone section beneath 2.4 km of confining material; the unconformity was placed at a depth of 4.8 km.

The results of these calculations are summarized in figure 29 for the case of ore formation by a solitary free convection cell. The ore zone itself is characterized by precipitation of uraninite, hematite, muscovite, and chlorite. Below this zone, alteration consists of hematite and quartz dissolution, with pyrite and chlorite precipitated. An outer halo of alteration surrounds the deposit within the sandstone. Hematite, muscovite, chlorite, and quartz form at the expense of K-feldspar. This observed pattern of alteration strongly resembles several unconformity-type uranium deposits (figs. 3–5). Based on a calculated groundwater velocity of approx 1 m/yr, nearly 500,000 yrs are required to produce the alteration halo. Subsequently, the pattern of alteration remains relatively unchanged, although uranium continues to precipitate near the unconformity.

Formation of significant uranium ore below the unconformity is not predicted by this model, although many deposits consist partially or entirely of sub-unconformity pitchblende (for example, Key Lake, Koongarra). This could be due to a variety of factors: the calculated flow pattern, based on an assumed hydrostratigraphic configuration; starting

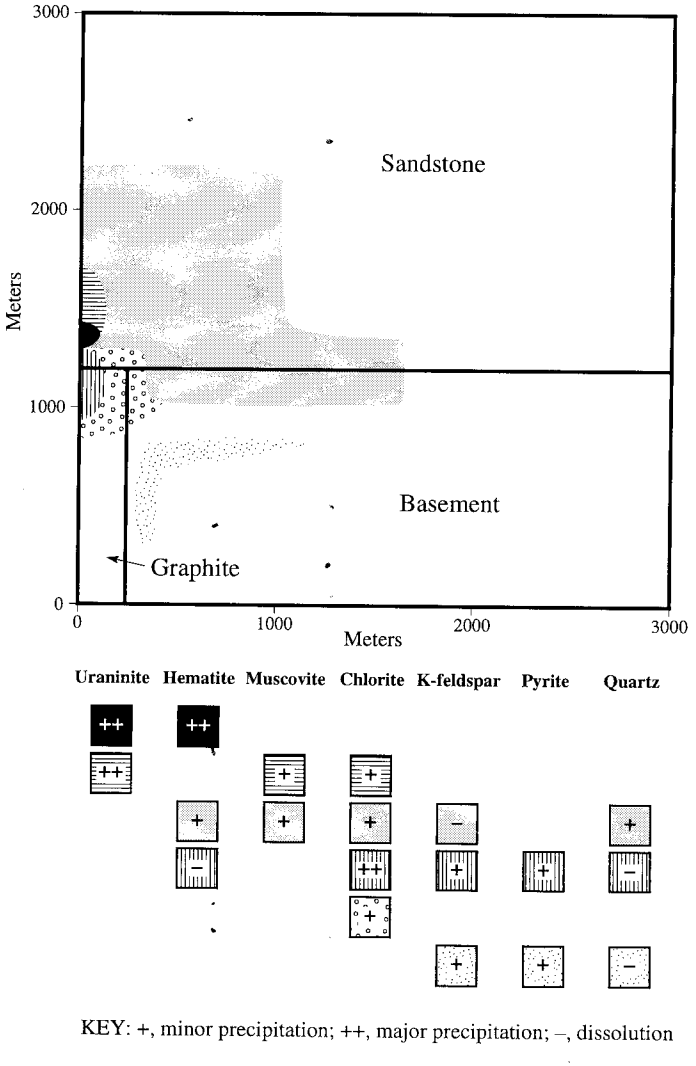

Fig. 29. Summary of calculated zones of alteration surrounding an unconformity-type uranium deposit. See discussion in text for an explanation of the alteration zones.

redox conditions in the basement and graphite units; the premise of a uranium source within the sandstone. More simulations are required to examine the influence of different starting conditions and flow geometries on the formation of an ore deposit. In general, however, these calculations confirm the hypothesis that significant quantities of uranium ore may be generated near the unconformity by groundwater flow due to free convection. In fact, based on results from other simulations, the

pattern of alteration observed to be associated with these ores is most likely produced by this mechanism.

Based on the results of this study, we can conclude the following:

1. Free convection within thick sandstones, such as those sequences found within the Athabasca and McArthur Basins, is a viable hydrochemical mechanism for the formation of unconformity-type uranium ores.
2. Moderate concentrations of aqueous uranium (less than 30 ppm) are sufficient to produce significant quantities of ore over a time scale of 0.1 to 1 Ma. Larger concentrations, possibly derived from leaching of volcanics within the sandstone sequence, may have produced an ore deposit in a shorter time.
3. Speciation calculations, using concentrations of chloride known from fluid inclusion studies of ore-related minerals, indicate that chloride complexes are the predominant form of aqueous uranium transported within the basin. Reactive transport calculations demonstrate that, if carbonate concentrations are sufficient within the sandstone to produce a predominance of uranyl-carbonate complexes, rutherfordine will precipitate within the sandstone. This further strengthens the conclusion that uranyl-chloride complexes were the most likely form of transported aqueous uranium in Proterozoic ore genesis.
4. Basement permeability and redox potential exert a strong influence on the formation of unconformity-type uranium ore deposits. The contrast in permeability between basement and graphite-rich fractured basement provides for focusing of groundwater flow upward within the graphite unit. As a result, reducing conditions exist within the sandstone near the unconformity. Although flow rates are only mm/yr within the basement, this small flux is important in forming an ore deposit. Extreme reducing conditions within the basement rocks lead to the precipitation of uraninite along a wide zone, in fact, across the entire length of the unconformity. High carbonate contents within the basement rocks lead to the precipitation of carbonate gangue minerals within the alteration halo. Although siderite is sometimes associated with these deposits, it is a minor component (Mellinger, Quirt, and Hoeve, 1987).
5. Changes in mass composition associated with the alteration halos around the ore deposits are the result of mass transport through temperature gradients and across compositional boundaries. For example, magnesium is brought into the basin flow system by groundwater flow through the basement (which contains significant quantities of Mg minerals) and precipitated as chlorite near the unconformity as fluids become warmed and low-potassium-content basin fluids are encountered. Quartz is dissolved below the ore deposit where fluids are being warmed and precipitated by cooling above the unconformity.

6. The modeling results indicate that in order to achieve observed patterns of ore mineralization and alteration, the graphite zone and zone of upward groundwater flow must coincide in space.
7. Finally, this study demonstrates that complex two-dimensional patterns of diagenesis and ore formation can be simulated through numerical solution of the equations describing groundwater flow and the resulting transport of thermal energy and multicomponent reactive solute mass in a sedimentary basin. Although some issues remain unresolved, such as the hydrologic flow field producing mineralization below the unconformity, this study has provided some insight into the hydrologic and geochemical processes responsible for unconformity-type uranium deposits.

ACKNOWLEDGMENTS

This study benefited from discussions with Ali Komninou, Tom Kotzer, Kurt Kyser, David Quirt, and Dimitri Sverjensky. We gratefully acknowledge the assistance of Nick Andrade and the Cigar Lake Mining Corporation, who allowed us access to the mine, and Peter Duerden and the Australian Nuclear Science and Technology Organisation, for providing travel to Koongarra. We would also like to thank L. Edmond Eary and Carl Steefel for helpful reviews. This work has been supported by the U.S. Nuclear Regulatory Commission (NRC grants NRC-04-89-108 and NRC-04-91-097 to G. Garven) and a Horton Research Grant from the Hydrology Division of the American Geophysical Union to J. Raffensperger.

APPENDIX I

Finite element equations for reactive solute transport

The simulations of groundwater flow, heat transport, and reactive solute transport were performed using a finite element code developed for this study. The methods employed for groundwater flow and heat transport solutions are described elsewhere (Raffensperger, ms) and are similar to those used in other studies (Garven, 1989). However, the solution approach for multicomponent reactive solute transport is new. The general transport relation takes the form:

$$\nabla \cdot (\phi \mathbf{D} \nabla M^T_{c,aq}) - \phi \mathbf{v} \cdot \nabla M^T_{c,aq} = \frac{\partial \phi M^T_c}{\partial t} \tag{1.1}$$

where terms of the dispersion tensor (**D**) are calculated for two-dimensional transport as (Pickens and Lennox, 1976):

$$D_{xx} = \alpha_L \frac{v_x^2}{|\mathbf{v}|} + \alpha_T \frac{v_z^2}{|\mathbf{v}|} + D^*$$

$$D_{zz} = \alpha_L \frac{v_z^2}{|\mathbf{v}|} + \alpha_T \frac{v_x^2}{|\mathbf{v}|} + D^*$$

$$D_{xz} = D_{zx} = (\alpha_L - \alpha_T) \frac{v_x v_z}{|\mathbf{v}|}$$

in which α_L and α_T are the longitudinal and transverse dispersivity, respectively, and D^* is the effective molecular diffusivity. The porous medium is assumed to be isotropic with respect to dispersivity. We may define the trial function:

$$C \approx \hat{C} = \sum_{m=1}^{N} C_m \xi_m \tag{1.2}$$

where C refers to concentration (either M_c^T or $M_{c,aq}^T$). The weighted residual equation may be written:

$$\iint_R \left[\nabla \cdot (\phi \mathbf{D} \nabla \hat{C}) - \phi \mathbf{v} \cdot \nabla \hat{C} - \frac{\partial \phi \hat{C}}{\partial t}\right] \xi_n \, dR = 0 \tag{1.3}$$

Simplifying and applying Green's theorem, this becomes:

$$\iint_R \phi \mathbf{D} \nabla \hat{C} \cdot \nabla \xi_n \, dR - \int_S \phi \mathbf{D} \nabla \hat{C} \cdot \mathbf{n} \xi_n \, dS + \iint_R \phi \mathbf{v} \cdot \nabla \hat{C} \xi_n \, dR + \iint_R \frac{\partial \phi \hat{C}}{\partial t} \xi_n \, dR = 0 \tag{1.4}$$

Rearranging and writing each integral as the summation over all the individual element subregions:

$$\sum_e \left(\iint_{R^e} \phi \mathbf{D}^e \nabla^e \hat{C} \cdot \nabla \xi_n^e \, dR^e + \iint_{R^e} \phi \mathbf{v}^e \cdot \nabla^e \hat{C} \xi_n^e \, dR^e + \iint_{R^e} \frac{\partial \phi^e \hat{C}}{\partial t} \xi_n^e \, dR^e \right) = \sum_e \left(\int_{S^e} \phi \mathbf{D}^e \nabla^e \hat{C} \cdot \mathbf{n} \xi_n^e \, dS^e \right) \tag{1.5}$$

Incorporating the trial function (1.2), replacing the right hand side of (1.5) with a flux term (Fick's first law):

$$\mathbf{J} = -\mathbf{D} \nabla C \tag{1.6}$$

(1.5) becomes:

$$\sum_m \left(\sum_e \iint_{R^e} \phi^e \mathbf{D}^e \nabla \xi_m^e \cdot \nabla \xi_n^e \, dR^e + \sum_e \iint_{R^e} \phi^e \mathbf{v}^e \cdot \nabla \xi_m^e \cdot \xi_n^e \, dR^e \right) C_m + \sum_m \left(\sum_e \iint_{R^e} \phi^e \xi_m^e \xi_n^e \, dR^e \right) \frac{dC_m}{dt} = -\sum_e \left(\int_{S^e} \phi^e \mathbf{J}^e \cdot \mathbf{n} \xi_n^e \, dS^e \right) \tag{1.7}$$

The summation over m is over all the nodes, and the summation over e is over all the elements. Evaluating the integrals and replacing C with the respective concentrations, (1.7) may be written in matrix notation:

$$E_{nm}(M_{c,aq}^T)_m + F_{nm} \frac{d(M_c^T)_m}{dt} = -G_n \qquad m, n = 1, \ldots, N \tag{1.8}$$

where N is the number of nodes, and:

$$E_{nm} = \sum_e E^e_{nm} = \sum_e \frac{\phi^e}{4\Delta}\left(D^e_{xx}\beta_n\beta_m + D^e_{xz}\beta_n\gamma_m + D^e_{zx}\gamma_n\beta_m + D^e_{zz}\gamma_n\gamma_m\right) + \sum_e \frac{\phi^e}{6}\left(v^e_x\beta_m + v^e_z\gamma_m\right)$$

$$F_{nm} = \sum_e \phi^e \begin{cases} \dfrac{\Delta}{6} & \text{for } n = m \\ \dfrac{\Delta}{12} & \text{for } n \neq m \end{cases}$$

$$G_n = -\sum_e \left(\frac{\phi^e M^T_{c,aq} l^e}{2}\right)$$

The coefficients γ and β are shape functions for linear triangular finite elements (Zienkiewicz, 1977):

$$\beta_1 = z_2 - z_3 \qquad \gamma_1 = x_3 - x_2$$
$$\beta_2 = z_3 - z_1 \qquad \gamma_2 = x_1 - x_3$$
$$\beta_3 = z_1 - z_2 \qquad \gamma_3 = x_2 - x_1$$

and Δ is the triangular element area:

$$2\Delta = \gamma_3\beta_1 - \gamma_1\beta_2$$

For this study, an alternative to sequential iteration was sought that would allow large-scale calculations to be carried out with execution speed comparable to a non-iterative explicit scheme, but that would be unconditionally stable. A two-step predictor-corrector scheme offered such an alternative. Compared with explicit or implicit methods, the predictor-corrector scheme offers several advantages for the numerical solution of nonlinear differential equations (Douglas and Jones, 1963). The predictor-corrector solution is second-order accurate, whereas explicit solutions are only first-order accurate. Therefore, a significant increase in accuracy can be obtained at the expense of doubling the computational effort at each time step. Since the explicit scheme is conditionally stable, relatively small time steps are required; the predictor-corrector scheme, on the other hand, can be shown to be unconditionally stable. Therefore, since this implies a significant reduction in the number of time steps required to maintain a prescribed accuracy, the use of the predictor-corrector scheme can dramatically reduce the computational effort. Implicit solutions are also second-order accurate but require iteration within a time step (Yeh and Tripathi, 1989, 1991). The disadvantage of the predictor-corrector scheme is that, when using large time step sizes, the extrapolation assumed (eq 1.12 below) may produce inaccuracies.

The predictor-corrector scheme is implemented as follows. We may rewrite (1.8) as:

$$E_{nm}(M^T_c)_m + F_{nm}\frac{d(M^T_c)_m}{dt} = E_{nm}(M^T_{c,sol})_m - G_n \tag{1.9}$$

The predictor-corrector algorithm consists of two steps. In the first step, an implicit scheme is used to solve for $(M^T_c)_m$ at the $k + \frac{1}{2}$ time step, using values of $(M^T_{c,sol})_m$ from the previous time step. This is analogous to assuming $d(M^T_{c,sol})_m/dt = 0$. The matrix expression for the predictor step may be written:

$$\left(E_{nm} + \frac{F_{nm}}{\Delta t/2}\right)(M^T_c)^{k+1/2}_m = E_{nm}(M^T_{c,sol})^k_m + \frac{F_{nm}}{\Delta t/2}(M^T_c)^k_m - G_n \tag{1.10}$$

This expression is solved directly using Gaussian elimination, after imposing Dirichlet (constant $M^T_{c,aq}$) boundary conditions. The chemical speciation is then recalculated to obtain

values for $(M^T_{c,sol})_m$ at the $k + \frac{1}{2}$ time step. The corrector step consists of a time-centered (Crank-Nicolson) scheme which uses a linear extrapolation of the change in solid concentration from time step k to time step $k + \frac{1}{2}$ to obtain a corrected estimate of $(M^T_{c,sol})_m$ at the $k + 1$ time step:

$$\left(\frac{E_{nm}}{2} + \frac{F_{nm}}{\Delta t}\right)(M^T_c)^{k+1}_m = \left(-\frac{E_{nm}}{2} + \frac{F_{nm}}{\Delta t}\right)(M^T_c)^k_m + \frac{E_{nm}}{2}[2(M^T_{c,sol})^{k+1/2}_m] - G_n \qquad (1.11)$$

After imposing the boundary conditions, this equation is solved for $(M^T_c)_m$ at the new time step $(k + 1)$. The extrapolation scheme assumes the following:

$$(M^T_{c,sol})^{k+1}_m - (M^T_{c,sol})^{k+1/2}_m = (M^T_{c,sol})^{k+1/2}_m - (M^T_{c,sol})^k_m \qquad (1.12)$$

In other words, the rate of precipitation or dissolution is approximately constant over a time step. If no precipitation or dissolution occurs, the approximation is trivially satisfied.

The predictor-corrector scheme has been tested for a variety of grid resolutions and time-step sizes, in both one and two dimensions (Raffensperger, ms). Results compare favorably with those produced using sequential iteration, indicating the accuracy of the scheme. For a one-dimensional problem, the number of iterations (per time step) required for the sequential iteration approach varied from 4 to more than 20, depending on the time step size. The efficiency of the predictor-corrector scheme allows complex problems to be solved within reasonable periods of computer time. Typically, the simulations presented in this study required between 40 and 160 CPU hours on an IBM RS6000, Model 560, rated at 31 MFLOPS.

Appendix 2

Thermodynamic Data

In this study, all the thermodynamic properties of the aqueous species and solids were calculated using the computer program SUPCRT, which calculates (in addition to thermodynamic properties of reaction) the logarithm of the equilibrium constant for any input reaction (Johnson, Oelkers, and Helgeson, 1992). In order to do this, a set of equation of state coefficients are required. For all non-uranium-bearing aqueous species and complexes, these coefficients are from Shock and Helgeson (1988). For the uranium-bearing species, these coefficients were regressed from available thermodynamic data. Thermodynamic data for the free uranium species U^{3+}, U^{4+}, UO_2^+, and UO_2^{2+} are taken from Grenthe and others (1990). Additional data on heat capacity and volume for UO_2^{2+} are from Hovey, Nguyen-Trung, and Tremaine (1989). For these species, equation of state coefficients were regressed or estimated (Shock and Helgeson, 1988). In order to obtain equation of state coefficients for aqueous uranium complexes using the approach described by Sverjensky (1987), dissociation constants (log K) at 25°C were required. Actual measurements were found for only a few complexes; therefore, estimates based on the unified theory of metal ion complexation (Brown and Wanner, 1987) were used when available.

Solubility products for all minerals were also calculated using SUPCRT. Gibbs free energies were calculated for most aluminosilicate and carbonate minerals using the model for heat capacities and data from Berman (1988) and revised data from Sverjensky, Hemley, and D'Angelo (1991). For other minerals, Gibbs free energies were calculated using data from Helgeson and others (1978). For uraninite and rutherfordine, data were available in the compilation by Grenthe and others (1990).

The log(K) values for a range of temperatures (25°-300°C) were fitted with a second order polynomial expression. Tables 2.1 and 2.2 list the complete set of coefficients describing the logarithm of the equilibrium constants for all aqueous and solid species in the

TABLE 2.1

Coefficients of polynomial used to calculate log(K) for aqueous species and complexes

Species	Reaction	σ_0	σ_1	σ_2
H^+	$H^+ + OH^- \Leftrightarrow H_2O$	−14.6	0.0280	-5.94×10^{-5}
O_2^0	$O_2^0 + \frac{1}{2}CH_4^0 + OH^- \Leftrightarrow \frac{1}{2}CO_3^{2-} + \frac{3}{2}H_2O$	86.4	−0.254	3.22×10^{-4}
HCl^0	$HCl^0 + OH^- \Leftrightarrow H_2O + Cl^-$	15.4	−0.0270	3.13×10^{-5}
CO_2^0	$CO_2^0 + 2OH^- \Leftrightarrow H_2O + CO_3^{2-}$	12.4	−0.0480	5.30×10^{-5}
HCO_3^-	$HCO_3^- + OH^- \Leftrightarrow H_2O + CO_3^{2-}$	4.15	−0.0220	2.58×10^{-5}
HSO_4^-	$HSO_4^- + OH^- \Leftrightarrow H_2O + SO_4^{2-}$	12.9	−0.0410	5.05×10^{-5}
HS^-	$HS^- + CO_3^{2-} + 2H_2O \Leftrightarrow SO_4^{2-} + CH_4^0 + OH^-$	−9.93	0.0200	-1.90×10^{-5}
H_2S^0	$H_2S^0 + CO_3^{2-} + H_2O \Leftrightarrow SO_4^{2-} + CH_4^0$	−2.52	0.00154	1.02×10^{-6}
$HSiO_3^-$	$HSiO_3^- \Leftrightarrow SiO_2^0 + OH^-$	−4.27	0.0120	-1.40×10^{-5}
$HFeO_2^-$	$HFeO_2^- + \frac{15}{8}H_2O + \frac{1}{8}CO_3^{2-} \Leftrightarrow Fe^{3+} + \frac{34}{8}OH^- + \frac{1}{8}CH_4^0$	−34.4	0.0330	-1.15×10^{-4}
$NaOH^0$	$NaOH^0 \Leftrightarrow Na^+ + OH^-$	0.256	−0.00291	-1.28×10^{-5}
$NaCl^0$	$NaCl^0 \Leftrightarrow Na^+ + Cl^-$	0.818	−0.00196	-1.38×10^{-5}
$NaHCO_3^0$	$NaHCO_3^0 + OH^- \Leftrightarrow Na^+ + H_2O + CO_3^{2-}$	3.93	−0.0190	7.44×10^{-6}
$NaHSiO_3^0$	$NaHSiO_3^0 \Leftrightarrow Na^+ + SiO_2^0 + OH^-$	−6.11	0.0200	-4.04×10^{-5}
KOH^0	$KOH^0 \Leftrightarrow K^+ + OH^-$	0.573	−0.00368	-9.16×10^{-6}
KCl^0	$KCl^0 \Leftrightarrow K^+ + Cl^-$	2.23	−0.00773	-3.74×10^{-6}
KSO_4^-	$KSO_4^- \Leftrightarrow K^+ + SO_4^{2-}$	−0.825	−0.00176	-1.93×10^{-5}
$KHSO_4^0$	$KHSO_4^0 + OH^- \Leftrightarrow K^+ + H_2O + SO_4^{2-}$	14.8	−0.0470	4.45×10^{-5}
$CaCl^+$	$CaCl^+ \Leftrightarrow Ca^{2+} + Cl^-$	0.774	−0.00223	-2.19×10^{-5}
$CaCl_2^0$	$CaCl_2^0 \Leftrightarrow Ca^{2+} + 2Cl^-$	0.641	0.00180	-4.87×10^{-5}
$CaCO_3^0$	$CaCO_3^0 \Leftrightarrow Ca^{2+} + CO_3^{2-}$	−3.22	−0.00575	-2.95×10^{-5}
$CaHCO_3^+$	$CaHCO_3^+ + OH^- \Leftrightarrow Ca^{2+} + H_2O + CO_3^{2-}$	3.20	−0.0240	8.13×10^{-7}
$CaSO_4^0$	$CaSO_4^0 \Leftrightarrow Ca^{2+} + SO_4^{2-}$	−2.10	−0.000816	-3.15×10^{-5}
$MgOH^+$	$MgOH^+ \Leftrightarrow Mg^{2+} + OH^-$	−2.12	−0.00349	-1.62×10^{-5}
MgO^0	$MgO^0 + H_2O \Leftrightarrow Mg^{2+} + 2OH^-$	−3.06	−0.0110	-2.86×10^{-5}
$MgCl^+$	$MgCl^+ \Leftrightarrow Mg^{2+} + Cl^-$	0.216	−0.00160	-2.63×10^{-5}
$MgCO_3^0$	$MgCO_3^0 \Leftrightarrow Mg^{2+} + CO_3^{2-}$	−2.96	−0.00189	-3.42×10^{-5}
$MgHCO_3^+$	$MgHCO_3^+ + OH^- \Leftrightarrow Mg^{2+} + H_2O + CO_3^{2-}$	3.23	−0.0250	3.02×10^{-6}
U^{3+}	$U^{3+} + \frac{3}{4}CO_3^{2-} + \frac{1}{4}OH^- + \frac{5}{8}H_2O \Leftrightarrow UO_2^{2+} + \frac{3}{8}CH_4^0$	19.2	−0.0390	7.20×10^{-5}
U^{4+}	$U^{4+} + \frac{1}{4}CO_3^{2-} + \frac{3}{4}OH^- \Leftrightarrow UO_2^{2+} + \frac{1}{4}CH_4^0 + \frac{1}{4}H_2O$	21.6	−0.00431	4.76×10^{-5}
UCl^{3+}	$UCl^{3+} + \frac{1}{4}CO_3^{2-} + \frac{3}{4}OH^- \Leftrightarrow UO_2^{2+} + Cl^- + \frac{1}{4}CH_4^0 + \frac{1}{4}H_2O$	20.3	−0.01000	-3.04×10^{-5}
UCl_2^{2+}	$UCl_2^{2+} + \frac{1}{4}CO_3^{2-} + \frac{3}{4}OH^- \Leftrightarrow UO_2^{2+} + 2Cl^- + \frac{1}{4}CH_4^0 + \frac{1}{4}H_2O$	22.3	−0.0750	-1.94×10^{-4}
$UHCO_3^{3+}$	$UHCO_3^{3+} + \frac{5}{4}OH^- \Leftrightarrow UO_2^{2+} + \frac{3}{4}CO_3^{2-} + \frac{1}{4}CH_4^0 + \frac{5}{4}H_2O$	18.6	0.00830	-7.13×10^{-5}
$U(HCO_3)_2^{2+}$	$U(HCO_3)_2^{2+} + \frac{7}{4}OH^- \Leftrightarrow UO_2^{2+} + \frac{7}{4}CO_3^{2-} + \frac{1}{4}CH_4^0 + \frac{9}{4}H_2O$	19.1	−0.0330	-3.61×10^{-4}
UO_2^+	$UO_2^+ + \frac{1}{8}CO_3^{2-} + \frac{7}{8}H_2O \Leftrightarrow UO_2^{2+} + \frac{1}{8}CH_4^0 + \frac{5}{4}OH^-$	−14.7	0.0240	-4.81×10^{-5}
UO_2Cl^0	$UO_2Cl^0 + \frac{1}{8}CO_3^{2-} + \frac{7}{8}H_2O \Leftrightarrow UO_2^{2+} + Cl^- + \frac{1}{8}CH_4^0 + \frac{5}{4}OH^-$	−15.1	0.0330	-6.53×10^{-5}
$UO_2Cl_2^-$	$UO_2Cl_2^- + \frac{1}{8}CO_3^{2-} + \frac{7}{8}H_2O \Leftrightarrow UO_2^{2+} + 2Cl^- + \frac{1}{8}CH_4^0 + \frac{5}{4}OH^-$	−15.2	0.0440	-7.41×10^{-5}
$UO_2HCO_3^0$	$UO_2HCO_3^0 \Leftrightarrow UO_2^{2+} + \frac{7}{8}CO_3^{2-} + \frac{1}{8}CH_4^0 + \frac{1}{8}H_2O + \frac{1}{4}OH^-$	−12.0	0.0130	-4.35×10^{-5}
$UO_2(HCO_3)_2^-$	$UO_2(HCO_3)_2^- + \frac{3}{4}OH^- \Leftrightarrow UO_2^{2+} + \frac{15}{8}CO_3^{2-} + \frac{1}{8}CH_4^0 + \frac{9}{8}H_2O$	−7.81	0.00180	-3.55×10^{-5}
UO_2Cl^+	$UO_2Cl^+ \Leftrightarrow UO_2^{2+} + Cl^-$	0.0880	−0.00776	-2.76×10^{-5}
$UO_2Cl_2^0$	$UO_2Cl_2^0 \Leftrightarrow UO_2^{2+} + 2Cl^-$	1.61	−0.0150	-5.51×10^{-5}
$UO_2CO_3^0$	$UO_2CO_3^0 \Leftrightarrow UO_2^{2+} + CO_3^{2-}$	−9.63	−0.000278	-3.62×10^{-5}
$UO_2HCO_3^+$	$UO_2HCO_3^+ + OH^- \Leftrightarrow UO_2^{2+} + CO_3^{2-} + H_2O$	0.443	−0.0150	-2.32×10^{-5}
$UO_2(HCO_3)_2^0$	$UO_2(HCO_3)_2^0 + 2OH^- \Leftrightarrow UO_2^{2+} + 2CO_3^{2-} + 2H_2O$	1.89	−0.0300	-4.54×10^{-5}
$UO_2SO_4^0$	$UO_2SO_4^0 \Leftrightarrow UO_2^{2+} + SO_4^{2-}$	−2.97	−0.00836	-2.51×10^{-5}
$UO_2HSO_4^+$	$UO_2HSO_4^+ + OH^- \Leftrightarrow UO_2^{2+} + H_2O + SO_4^{2-}$	9.94	−0.0350	1.16×10^{-6}
$AlOH^{2+}$	$AlOH^{2+} \Leftrightarrow Al^{3+} + OH^-$	−9.01	0.00209	-2.50×10^{-5}
$AlCl^{2+}$	$AlCl^{2+} \Leftrightarrow Al^{3+} + Cl^-$	−0.931	0.000414	-3.21×10^{-5}
$AlCl_2^+$	$AlCl_2^+ \Leftrightarrow Al^{3+} + 2Cl^-$	−1.58	0.00399	-7.81×10^{-5}
$FeCl^{2+}$	$FeCl^{2+} \Leftrightarrow Fe^{3+} + Cl^-$	−0.957	−0.000884	-2.83×10^{-5}
Fe^{2+}	$Fe^{2+} + \frac{1}{8}CO_3^{2-} + \frac{7}{8}H_2O \Leftrightarrow Fe^{3+} + \frac{1}{8}CH_4^0 + \frac{5}{4}OH^-$	−26.5	0.0400	-8.14×10^{-5}
$FeOH^+$	$FeOH^+ + \frac{1}{8}CO_3^{2-} + \frac{7}{8}H_2O \Leftrightarrow Fe^{3+} + \frac{1}{8}CH_4^0 + \frac{9}{4}OH^-$	−29.7	0.0410	-1.04×10^{-4}
FeO^0	$FeO^0 + \frac{1}{8}CO_3^{2-} + \frac{15}{8}H_2O \Leftrightarrow Fe^{3+} + \frac{1}{8}CH_4^0 + \frac{13}{4}OH^-$	−33.5	0.0410	-1.25×10^{-4}
$FeCl^+$	$FeCl^+ + \frac{1}{8}CO_3^{2-} + \frac{7}{8}H_2O \Leftrightarrow Fe^{3+} + Cl^- + \frac{1}{8}CH_4^0 + \frac{5}{4}OH^-$	−26.3	0.0380	-1.03×10^{-4}
$FeCl_2^0$	$FeCl_2^0 + \frac{1}{8}CO_3^{2-} + \frac{7}{8}H_2O \Leftrightarrow Fe^{3+} + 2Cl^- + \frac{1}{8}CH_4^0 + \frac{5}{4}OH^-$	−23.8	0.0360	-1.25×10^{-4}
$FeHCO_3^+$	$FeHCO_3^+ \Leftrightarrow Fe^{3+} + \frac{7}{8}CO_3^{2-} + \frac{1}{8}CH_4^0 + \frac{1}{8}H_2O + \frac{1}{4}OH^-$	−23.6	0.0230	-8.85×10^{-5}

TABLE 2.2

Coefficients of polynomial used to calculate log(K) for minerals

Mineral	Reaction	σ_0	σ_1	σ_2
Halite	$NaCl \Leftrightarrow Na^+ + Cl^-$	1.54	0.00241	-2.00×10^{-5}
Albite	$NaAlSi_3O_8 + 2H_2O \Leftrightarrow Na^+ + 4OH^- + Al^{3+} + 3SiO_2^0$	−57.7	0.0870	-2.15×10^{-4}
Sylvite	$KCl \Leftrightarrow K^+ + Cl^-$	0.667	0.00911	-3.14×10^{-5}
K–feldspar	$KAlSi_3O_8 + 2H_2O \Leftrightarrow K^+ + 4OH^- + Al^{3+} + 3SiO_2^0$	−60.3	0.0990	-2.34×10^{-4}
Muscovite	$KAl_2(AlSi_3O_{10})(OH)_2 + 4H_2O \Leftrightarrow K^+ + 10OH^- + 3Al^{3+} + 3SiO_2^0$	−135	0.172	-4.79×10^{-4}
Calcite	$CaCO_3 \Leftrightarrow Ca^{2+} + CO_3^{2-}$	−8.14	−0.00650	-3.86×10^{-5}
Dolomite	$CaMg(CO_3)_2 \Leftrightarrow Ca^{2+} + Mg^{2+} + 2CO_3^{2-}$	−17.0	−0.0190	-6.78×10^{-5}
Anhydrite	$CaSO_4 \Leftrightarrow Ca^{2+} + SO_4^{2-}$	−4.05	−0.01000	-3.21×10^{-5}
Anorthite	$CaAl_2Si_2O_8 + 4H_2O \Leftrightarrow Ca^{2+} + 8OH^- + 2Al^{3+} + 2SiO_2^0$	−90.5	0.0810	-3.09×10^{-4}
Magnesite	$MgCO_3 \Leftrightarrow Mg^{2+} + CO_3^{2-}$	−8.05	−0.0150	-2.58×10^{-5}
Cordierite	$Mg_2Al_4Si_5O_{18} + 8H_2O \Leftrightarrow 5Mg^{2+} + 16OH^- + 4Al^{3+} + 5SiO_2^0$	−182	0.147	-5.94×10^{-4}
Chlorite	$Mg_5Al(AlSi_3O_{10})(OH)_8 + 4H_2O \Leftrightarrow 5Mg^{2+} + 16OH^- + 2Al^{3+} + 3SiO_2^0$	−169	0.171	-5.95×10^{-4}
Uraninite	$UO_2 + \frac{7}{4}H_2O + \frac{1}{4}CO_3^{2-} \Leftrightarrow UO_2^{2+} + \frac{1}{2}OH^- + \frac{1}{4}CH_4^0$	−40.8	0.0720	-1.44×10^{-4}
Rutherfordine	$UO_2CO_3 \Leftrightarrow UO_2^{2+} + CO_3^{2-}$	−14.1	−0.00653	-6.55×10^{-5}
Kaolinite	$Al_2Si_2O_5(OH)_4 + H_2O \Leftrightarrow 2Al^{3+} + 6OH^- + 2SiO_2^0$	−82.7	0.103	-2.86×10^{-4}
Hematite	$Fe_2O_3 + 3H_2O \Leftrightarrow 2Fe^{3+} + 6OH^-$	−85.6	0.103	-2.88×10^{-4}
Magnetite	$Fe_3O_4 + \frac{39}{8}H_2O + \frac{1}{8}CO_3^{2-} \Leftrightarrow 3Fe^{3+} + \frac{37}{4}OH^- + \frac{1}{8}CH_4^0$	−130	0.156	-4.33×10^{-4}
Siderite	$FeCO_3 + \frac{7}{8}H_2O \Leftrightarrow Fe^{3+} + \frac{5}{4}OH^- + \frac{7}{8}CO_3^{2-} + \frac{1}{8}CH_4^0$	−36.8	0.0300	-1.15×10^{-4}
Pyrite	$FeS_2 + \frac{41}{8}H_2O + \frac{15}{8}CO_3^{2-} \Leftrightarrow Fe^{3+} + \frac{11}{4}OH^- + 2SO_4^{2-} + \frac{15}{8}CH_4^0$	−66.1	0.125	-2.25×10^{-4}
Quartz	$SiO_2 \Leftrightarrow SiO_2^0$	−4.23	0.0130	-1.92×10^{-5}
Graphite	$C + \frac{1}{2}H_2O + OH^- \Leftrightarrow \frac{1}{2}CH_4^0 + \frac{1}{2}CO_3^{2-}$	0.998	−0.00365	8.44×10^{-6}

chemical system. These coefficients are used to calculate the $\log(K)$ according to the following relation:

$$\log K = \sigma_0 + \sigma_1 T + \sigma_2 T^2 \tag{2.1}$$

where T is temperature in °C.

In the chemical system used in the study, the redox state is defined by reference to the CO_3^{2-}–CH_4^0 redox couple. For this pair, we may write the reaction:

$$CO_3^{2-} + 7H_2O + 8e^- \Leftrightarrow CH_4^0 + 10OH^- \tag{2.2}$$

We may write the Nernst equation (Stumm and Morgan, 1981) for this reaction as:

$$E_H = E_H^0 + \frac{RT}{8F} \ln\left(\frac{a_{CO_3^{2-}}}{a_{CH_4^0} a_{OH^-}^{10}}\right) \tag{2.3}$$

The standard redox potential (E_H^0) is given by:

$$E_H^0 = -\frac{\Delta G_r^0}{8F} = \frac{RT}{8F} \ln K \tag{2.4}$$

where R is the gas constant, F is Faraday's constant, and T is temperature in °K. A fourth-order polynomial fit is used to calculate the logarithm of this equilibrium constant:

$$\log K = -108.8892 + 0.31577T - 0.00129T^2 + 304509 \times 10^{-6}T^3 - 3.64919 \times 10^{-9}T^4 \quad (2.5)$$

where T is temperature in °C.

References

Ague, J. J., and Brimhall, G. H., 1989, Geochemical modeling of steady state fluid flow and chemical reaction during supergene enrichment of porphyry copper deposits: Economic Geology, v. 84, p. 506–528.

Ayres, D. E., Wray, E. M., Farstad, J., and Ibrahim, H., 1983, Geology of the Midwest uranium deposit, *in* Cameron, E. M., editor, Uranium Exploration in Athabasca Basin, Saskatchewan: Geological Survey of Canada, Paper 82–11, p. 33–40.

Baadsgaard, H., Cumming, G. L., and Worden, J. M., 1984, U-Pb geochronology of minerals from the Midwest uranium deposit, northern Saskatchewan: Canadian Journal of Earth Sciences, v. 21, p. 642–648.

Bell, K., 1981, A review of the geochronology of the Precambrian of Saskatchewan—some clues to uranium mineralization: Mineralogical Magazine, v. 44, p. 371–378.

Berman, R. G., 1988, Internally-consistent thermodynamic data for minerals in the system Na_2O-K_2O-CaO-MgO-FeO-Fe_2O_3- Al_2O_3-SiO_2-TiO_2- H_2O-CO_2: Journal of Petrology, v. 29, p. 445– 522.

Boast, C. W., 1973, Modeling the movement of chemicals in soils by water: Soil Science, v. 115, 3, p. 224–230.

Bray, C. J., Spooner, E. T. C., Hall, C. M., York, D., Bills, T. M., and Krueger, H. W., 1987, Laser probe $^{40}Ar/^{39}Ar$ and conventional K/Ar dating of illites associated with the McClean unconformity-related uranium deposits, north Saskatchewan, Canada: Canadian Journal of Earth Sciences, v. 24, p. 10–23.

Bray, C. J., Spooner, E. T. C., and Longstaffe, F. J., 1988, Unconformity-related uranium mineralization, McClean deposits, north Saskatchewan, Canada: hydrogen and oxygen isotope geochemistry: Canadian Mineralogist, v. 26, no. 2, p. 249–268.

Brown, P. L., and Wanner, H., 1987, Predicted formation constants using the unified theory of metal ion complexation, Organisation for Economic Co-operation and Development. Nuclear Energy Agency, 102 p.

Bruneton, P., 1987, Geology of the Cigar Lake uranium deposit (Saskatchewan, Canada), *in* Gilboy, C. F., and Vigrass, L. W., editors, Economic Minerals of Saskatchewan: Saskatchewan Geological Society Special Publication 8, p. 99–119.

Burden, R. L., Faires, J. D., and Reynolds, A. C., 1981, Numerical Analysis, 2nd edition: Boston, Massachusetts, PWS Publishers, 598 p.

Carl, C., Hohndorf, A., von Pechmann, E., Strnad, J. G., and Ruhrmann, G., 1988, Geochronology of the Key Lake uranium deposit, Saskatchewan, Canada [abstract]: Chemical Geology, v. 70, no. 1/2, p. 133.

Carnahan, C. L., 1987, Simulation of chemically reactive solute transport under conditions of changing temperature, *in* Tsang, C.-F., editor, Coupled Processes Associated with Nuclear Waste Repositories: New York, Academic Press, p. 249–257.

Cederberg, G. A., Street, R. L., and Leckie, J. O., 1985, A groundwater mass transport and equilibrium chemistry model for multicomponent systems: Water Resources Research, v. 21, no. 8, p. 1095–1104.

Chu, S.-Y., and Sposito, G., 1980, A derivation of the macroscopic solute transport equation for homogeneous, saturated, porous media: Water Resources Research, v. 16, no. 3, p. 542–546.

Cumming, G. L., and Scott, B. P., 1976, Rb/Sr dating of rocks from the Wollaston Lake Belt, Saskatchewan: Canadian Journal of Earth Sciences, v. 13, p. 355–364.

Dahlkamp, F. J., 1978, Geologic appraisal of the Key Lake U-Ni deposits, northern Saskatchewan: Economic Geology, v. 73, p. 1430–1449.

———— 1979, Uranium occurrences in northern Saskatchewan, Canada, and their mode of origin: The Royal Society (London), Philosophical Transactions v. A 291, p. 369–384.

Derry, D. R., 1973, Ore deposition and contemporaneous surfaces: Economic Geology, v. 68, p. 1374–1380.

Douglas, J., and Jones, B. F., 1963, On predictor-corrector methods for nonlinear parabolic differential equations: Journal of the Society for Industrial and Applied Mathematics, v. 11, no. 1, p. 195–204.

Ewers, G. R., and Ferguson, J., 1980, Mineralogy of the Jabiluka, Ranger, Koongarra, and Nabarlek uranium deposits, *in* Ferguson, J., and Goleby, A. B., editors, Uranium in the Pine Creek Geosyncline, Proceedings of the International Uranium Symposium on the Pine Creek Geosyncline, Sydney, June 4–8, 1979: International Atomic Energy Agency, Vienna, Austria p. 363–374.

Ewers, G. R., Ferguson, J., and Donnelly, T. H., 1983, The Nabarlek uranium deposit, Northern Territory, Australia: some petrologic and geochemical constraints on genesis: Economic Geology, v. 78, p. 823–837.

Foy, M. F., and Pederson, C. P., 1975, Koongarra uranium deposit, *in* Knight, C. L., editor, Economic Geology of Australia and Papua New Guinea, 1. Metals: Australasian Institute of Mining and Metallurgy, p. 317–321.

Fryer, B. J., and Taylor, R. P., 1984, Sm-Nd direct dating of the Collins Bay hydrothermal uranium deposit, Saskatchewan: Geology, v. 12, p. 479–482.

Garven, G., 1989, A hydrogeologic model for the formation of the giant oil sands deposits of the Western Canada Sedimentary Basin: American Journal of Science, v. 289, p. 105–166.

Garven, G., and Freeze, R. A., 1984, Theoretical analysis of the role of groundwater flow in the genesis of stratabound ore deposits 1. Mathematical and numerical model: American Journal of Science, v. 284, p. 1085–1124.

Gelhar, L. W., Welty, C., and Rehfeldt, K. R., 1992, A critical review of data on field-scale dispersion in aquifers: Water Resources Research, v. 28, p. 1955–1974.

Grenthe, I., Fuger, J., Lemire, R. J., Muller, A. B., Nguyen-Trung, C., and Wanner, H., 1990, Chemical Thermodynamics of Uranium, Final Draft for Peer Review: Nuclear Energy Agency, 655 p.

Grove, D. B., and Stollenwerk, K. G., 1987, Chemical reactions simulated by ground-water-quality models: Water Resources Bulletin, v. 23, p. 601–615.

Gustafson, L. B., and Curtis, L. W., 1983, Post-Kombolgie metasomatism at Jabiluka, Northern Territory, Australia, and its significance in the formation of high-grade uranium mineralization in Lower Proterozoic rocks: Economic Geology, v. 78, p. 26–56.

Hanor, J. S., 1987, Origin and Migration of Subsurface Sedimentary Brines: Tulsa, Oklahoma, Society of Economic Paleontologists and Mineralogists, 247 p.

Hegge, M. R., and Rowntree, J. C., 1978, Geologic setting and concepts on the origin of uranium deposits in the East Alligator River region, N. T., Australia: Economic Geology, v. 73, p. 1420–1429.

Helgeson, H. C., 1968, Evaluation of irreversible reactions in geochemical processes involving minerals and aqueous solutions—I. Thermodynamic relations: Geochimica et Cosmochimica Acta, v. 32, p. 853–877.

———— 1969, Thermodynamics of hydrothermal systems at elevated temperatures and pressures: American Journal of Science, v. 267, p. 729–804.

Helgeson, H. C., Brown, T. H., Nigrini, A., and Jones, T. A., 1970, Calculation of mass transfer in geochemical processes involving aqueous solutions: Geochimica et Cosmochimica Acta, v. 34, p. 569–592.

Helgeson, H. C., Delany, J. M., Nesbitt, H. W., and Bird, D. K., 1978, Summary and critique of the thermodynamic properties of rock-forming minerals: American Journal of Science, v. 278-A, p. 1–220.

Helgeson, H. C., Kirkham, D. H., and Flowers, G. C., 1981, Theoretical prediction of the thermodynamic behavior of aqueous electrolytes at high pressures and temperatures. IV. Calculation of activity coefficients, osmotic coefficients, apparent molal and standard and relative partial molal properties to 5 kb and 600°C: American Journal of Science, v. 281, p. 1241–1516.

Hoeve, J., 1984, Host rock alteration and its application as an ore guide at the Midwest Lake uranium deposit, northern Saskatchewan: CIM Bulletin, v. 77, no. 868, p. 63–72.

Hoeve, J., and Quirt, D., 1984, Mineralization and host rock alteration in relation to clay mineral diagenesis and evolution of the Middle-Proterozoic, Athabasca Basin, northern Saskatchewan, Canada, Saskatchewan Research Counsel Technical Report 187: 187 p.

———— 1987, A stationary redox front as a critical factor in the formation of high-grade, unconformity-type uranium ores in the Athabasca basin, Saskatchewan, Canada: Bulletin de Minéralogie, v. 110, p. 157–171.

Hoeve, J., and Sibbald, T. I. I., 1978, On the genesis of Rabbit Lake and other unconformity-type uranium deposits in northern Saskatchewan, Canada: Economic Geology, v. 73, p. 1450–1473.

Hoffman, P. F., 1989, Precambrian geology and tectonic history of North America, *in* Bally, A. W., and Palmer, A. R., editors, The Geology of North America–An Overview, The Geology of North America A: Boulder, Colorado, Geological Society of America, p. 447–512.

Hovey, J. K., Nguyen-Trung, C., and Tremaine, P. R., 1989, Thermodynamics of aqueous uranyl ion: apparent and partial molar heat capacities and volumes of aqueous uranyl perchlorate from 10 to 55°C: Geochimica et Cosmochimica Acta, v. 53, p. 1503–1509.

Isobe, H., Murakami, T., and Ewing, R. C., 1992, Alteration of uranium minerals in the Koongarra deposit, Australia: unweathered zone: Journal of Nuclear Materials, v. 190, p. 174–187.

Johnson, J. W., Oelkers, E. H., and Helgeson, H. C., 1992, SUPCRT92: a software package for calculating the standard molal thermodynamic properties of minerals, gases, aqueous species, and reactions from 1 to 5000 bar and 0 to 1000°C: Computers & Geosciences, v. 18, p. 899–947.

Kirkner, D. J., Theis, T. L., and Jennings, A. A., 1984, Multicomponent solute transport with sorption and soluble complexation: Advances in Water Resources, v. 7, p. 120–125.

Knapp, R. B., 1989, Spatial and temporal scales of local equilibrium in dynamic fluid-rock systems: Geochimica et Cosmochimica Acta, v. 53, p. 1955–1964.

Kotzer, T., and Kyser, T. K., 1990a, The use of stable and radiogenic isotopes in the identification of fluids and processes associated with unconformity-type uranium deposits, *in* Beck, L. S., and Harper, C. T., editors, Modern Exploration Techniques. Regina, Saskatchewan, Canada, Saskatchewan Geological Society, Special Publication 10, p. 115–131.

———— 1990b, Fluid history of the Athabasca Basin and its relation to uranium deposits, *in* Summary of Investigations 1990, Miscellaneous Report 90-4: Regina, Saskatchewan, Canada, Saskatchewan Geological Survey, Saskatchewan Energy and Mines, p. 153–157.

Kyser, T. K., Wilson, M. R., and Ruhrmann, G., 1989, Stable isotope constraints on the role of graphite in the genesis of unconformity-type uranium deposits: Canadian Journal of Earth Sciences, v. 26, p. 490–498.

Langford, F. F., 1974, A supergene origin for vein-type uranium ores in the light of the western Australian calcrete-carnotite deposits: Economic Geology, v. 69, p. 516–526.

———— 1977, Surficial origin of North American pitchblende and related uranium deposits: American Association of Petroleum Geologists Bulletin, v. 61, p. 28–42.

———— 1978, Origin of unconformity-type pitchblende deposits in the Athabasca Basin of Saskatchewan, *in* Kimberley, M. M., editor, Uranium Deposits, Their Mineralogy and Origin, Mineralogical Association of Canada Short Course Handbook Volume 3: Toronto, Canada, University of Toronto Press, p. 485–499.

Langmuir, D., 1987, Overview of coupled processes with emphasis in geochemistry, *in* Tsang, C.-F., editor, Coupled Processes Associated with Nuclear Waste Repositories: New York, Academic Press, p. 67–101.

Lichtner, P. C., 1985, Continuum model for simultaneous chemical reactions and mass transport in hydrothermal systems: Geochimica et Cosmochimica Acta, v. 49, p. 779–800.

———— 1992, Time-space continuum description of fluid/rock interaction in permeable media: Water Resources Research, v. 28, p. 3135–3155.

Lichtner, P. C., and Biino, G. G., 1992, A first principles approach to supergene enrichment of a prophyry copper protore: I. Cu-Fe-S subsystem: Geochimica et Cosmochimica Acta, v. 56, p. 3987–4013.

Liu, C. W., and Narasimhan, T. N., 1989, Redox-controlled multiple-species reactive chemical transport 2. Verification and application: Water Resources Research, v. 25, p. 883–910.

Ludwig, K. R., Grauch, R. I., Nutt, C. J., Nash, J. T., Frishman, D., and Simmons, K. R., 1987, Age of uranium mineralization at the Jabiluka and Ranger deposits, Northern Territory, Australia: new U-Pb isotope evidence: Economic Geology, v. 82, p. 857–874.

Maas, R., 1989, Nd-Sr isotope constraints on the age and origin of unconformity-type uranium deposits in the Alligator Rivers Uranium Field, Northern Territory, Australia: Economic Geology, v. 84, p. 64–90.

Mangold, D. C., and Tsang, C.-F., 1991, A summary of subsurface hydrological and hydrochemical models: Reviews of Geophysics, v. 29, p. 51–79.

Marle, C. M., 1982, On macroscopic equations governing multiphase flow with diffusion and chemical reactions in porous media: International Journal of Engineering Science, v. 20, p. 643–662.

Marmont, S., 1987, Ore deposit models #13. Unconformity-type uranium deposits: Geoscience Canada, v. 14, p. 219–229.

Marsily, G. de, 1986, Quantitative Hydrogeology. Marsily, G. de, translator: New York, Academic Press, Inc., 440 p.
McLennan, S. M., and Taylor, S. R., 1979, Rare earth element mobility associated with uranium mineralisation: Nature, v. 282, p. 247–250.
Mellinger, M., Quirt, D., and Hoeve, J., 1987, Geochemical signatures of uranium deposition in the Athabasca Basin of Saskatchewan, Canada: Uranium, v. 3, p. 187–209.
Mercer, J. W., and Faust, C. R., 1979, Geothermal reservoir simulation 3. Application of liquid- and vapor-dominated hydrothermal modeling techniques to Wairakei, New Zealand: Water Resources Research, v. 15, p. 653–671.
Miller, C. W., and Benson, L. V., 1983, Simulation of solute transport in a chemically reactive heterogeneous system: model development and application: Water Resources Research, v. 19, p. 381–391.
Money, P. L., 1968, The Wollaston Lake fold-belt system, Saskatchewan-Manitoba: Canadian Journal of Earth Sciences, v. 5, p. 1489–1504.
Nash, J. T., Granger, H. C., and Adams, S. S., 1981, Geology and concepts of important types of uranium deposits: Economic Geology, 75th Anniversary Volume, p. 63–116.
Needham, R. S., and Stuart-Smith, P. G., 1976, The Cahill Formation-host to uranium deposits in the Alligator Rivers Uranium Field, Australia: BMR Journal of Australian Geology & Geophysics, v. 1, p. 321–333.
Needham, R. S., Stuart-Smith, P. G., and Page, R. W., 1988, Tectonic evolution of the Pine Creek inlier, Northern Territory: Precambrian Research, v. 40/41, p. 543–564.
Nguyen, V. V., Gray, W. G., Pinder, G. F., Botha, J. F., and Crerar, D. A., 1982, A theoretical investigation on the transport of chemicals in reactive porous media: Water Resources Research, v. 18, p. 1149–1156.
Noorishad, J., Carnahan, C. L., and Benson, L. V., 1985, Development of a kinetic-equilibrium chemical transport code [abstract]: EOS, [Transactions, American Geophysical Union], v. 66, p. 274.
Nutt, C. J., 1989, Chloritization and associated alteration at the Jabiluka unconformity-type uranium deposit, Northern Territory, Australia: Canadian Mineralogist, v. 27, p. 41–58.
Oelkers, E. H., and Helgeson, H. C., 1990, Triple-ion anions and polynuclear complexing in supercritical electrolyte solutions: Geochimica et Cosmochimica Acta, v. 54, p. 727–738.
Ortoleva, P., Merino, E., Moore, C., and Chadam, J., 1987, Geochemical self-organization I: reaction-transport feedbacks and modeling approach: American Journal of Science, v. 287, p. 979–1007.
Percival, J. B. M., ms, 1989, Clay mineralogy, geochemistry, and partitioning of uranium within the alteration halo of the Cigar Lake uranium deposit, Saskatchewan, Canada: Ph.D. dissertation, Carleton University, Ottawa, Ontario, 343 p.
Percival, J. B., and Kodama, H., 1989, Sudoite from Cigar Lake, Saskatchewan: Canadian Mineralogist, v. 27, p. 633–641.
Philippe, S., and Lancelot, J., 1988, U-Pb geochronological investigation of the Cigar Lake U ore deposit, Saskatchewan [abstract]: Chemical Geology, v. 70, p. 135.
Phillips, O. M., 1991, Flow and Reactions in Permeable Rocks: New York, Cambridge University Press, 285 p.
Pickens, J. F., and Lennox, W. C., 1976, Numerical simulation of waste movement in steady groundwater flow systems: Water Resources Research, v. 12, p. 171–180.
Plumb, K. A., Derrick, G. M., Needham, R. S., and Shaw, R. D., 1981, The Proterozoic of northern Australia, *in* Hunter, D. R., editor, Precambrian of the Southern Hemisphere. Developments in Precambrian Geology 2: New York, Elsevier, p. 205–307.
Press, W. H., Flannery, B. P., Teukolsky, S. A., and Vetterling, W. T., 1986, Numerical Recipes: The Art of Scientific Computing: Cambridge, Cambridge University Press, 818 p.
Raffensperger, J. P., ms, 1993, Quantitative evaluation of the hydrologic and geochemical processes involved in the formation of unconformity-type uranium deposits: Ph.D. dissertation, The Johns Hopkins University, Baltimore, Maryland, 679 p.
Raffensperger, J. P., and Garven, Grant, 1995, The formation of unconformity-type uranium ore deposits. 1. Coupled groundwater flow and heat transport modeling: American Journal of Science, v. 295, p. 581–630.
Reed, M. H., 1982, Calculation of multicomponent chemical equilibria and reaction processes in systems involving minerals, gases and an aqueous phase: Geochimica et Cosmochimica Acta, v. 46, p. 513–528.
Rubin, J., 1983, Transport of reacting solutes in porous media: relation between mathematical nature of problem formulation and chemical nature of reactions: Water Resources Research, v. 19, p. 1231–1252.

Rubin, J., and James, R. V., 1973, Dispersion-affected transport of reacting solutes in saturated porous media: Galerkin method applied to equilibrium-controlled exchange in unidirectional steady water flow: Water Resources Research, v. 9, p. 1332–1356.

Ruhrmann, G., 1987, The Gaertner uranium orebody at Key Lake (northern Saskatchewan, Canada) after three years of mining: an update of the geology, *in* Gilboy, C. F., and Vigrass, L. W., editors, Economic Minerals of Saskatchewan, Special Publication Number 8: Regina, Saskatchewan, Canada, Saskatchewan Geological Society, p. 120–137.

Ryan, G. R., 1979, The genesis of Proterozoic uranium deposits in Australia: Philosophical Transactions of the Royal Society (London), v. A 291, p. 339–353.

Sanford, W. E., and Konikow, L. F., 1989, Simulation of calcite dissolution and porosity changes in saltwater mixing zones in coastal aquifers: Water Resources Research, v. 25, no. 4, p. 655–667.

Shock, E. L., and Helgeson, H. C., 1988, Calculation of the thermodynamic and transport properties of aqueous species at high pressures and temperatures: correlation algorithms for ionic species and equation of state predictions to 5 kb and 1000°C: Geochimica et Cosmochimica Acta, v. 52, p. 2009–2036.

Shock, E. L., Helgeson, H. C., and Sverjensky, D. A., 1989, Calculation of the thermodynamic and transport properties of aqueous species at high pressures and temperatures: standard partial molal properties of inorganic neutral species: Geochimica et Cosmochimica Acta, v. 53, p. 2157–2183.

Snelling, A. A., 1980, Uraninite and its alteration products, Koongarra uranium deposit, *in* Ferguson, J., and Goleby, A. B., editors, Uranium in the Pine Creek Geosyncline, Proceedings of the International Uranium Symposium on the Pine Creek Geosyncline, Sydney, June 4–8, 1979: International Atomic Energy Agency, p. 487–498 Vienna, Austria.

Steefel, C. I., and Lasaga, A. C., 1992, Putting transport into water-rock interaction models: Geology, v. 20, p. 680–684.

———— 1994, A coupled model for transport of multiple chemical species and kinetic precipitation/dissolution reactions with application to reactive flow in single phase hydrothermal systems: American Journal of Science, v. 294, p. 529–592.

Stumm, W., and Morgan, J. J., 1981, Aquatic Chemistry: An Introduction Emphasizing Chemical Equilibria in Natural Waters, 2d edition: New York, John Wiley & Sons, 780 p.

Sverjensky, D. A., 1987, Calculation of the thermodynamic properties of aqueous species and the solubilities of minerals in supercritical electrolyte solutions, *in* Carmichael, I. S. E., and Eugster, H. P., editors, Thermodynamic Modeling of Geologic Materials: Minerals, Fluids, Melts: Mineralogical Society of America, Reviews in Mineralogy 17, p. 177–209.

Sverjensky, D. A., Hemley, J. J., and D'Angelo, W. M., 1991, Thermodynamic assessment of hydrothermal alkali feldspar-mica-aluminosilicate equilibria: Geochimica et Cosmochimica Acta, v. 55, p. 989–1004.

Tremblay, L. P., 1982, Geology of the uranium deposits related to the sub-Athabasca unconformity, Saskatchewan: Geological Survey of Canada, Paper 81-20, 56 p.

Trocki, L. K., Curtis, D. B., Gancarz, A. J., and Banar, J. C., 1984, Ages of major uranium mineralization and lead loss in the Key Lake uranium deposit, northern Saskatchewan, Canada: Economic Geology, v. 79, p. 1378–1386.

Walsh, M. P., ms, 1983, Geochemical flow modeling: Ph.D. dissertation, University of Texas, Austin, 502 p.

Walsh, M. P., Bryant, S. L., Schechter, R. S., and Lake, L. W., 1984, Precipitation and dissolution of solids attending flow through porous media: American Institute of Chemical Engineers Journal, v. 30, p. 317–328.

Wilde, A. R., ms, 1988, On the origin of unconformity-related uranium deposits: Ph.D. dissertation, Monash University, Clayton, Victoria, Australia, 226 p.

Wilde, A. R., and Wall, V. J., 1987, Geology of the Nabarlek uranium deposit, Northern Territory, Australia: Economic Geology, v. 82, p. 1152–1168.

Yeh, G. T., and Tripathi, V. S., 1989, A critical evaluation of recent developments in hydrogeochemical transport models of reactive multichemical components: Water Resources Research, v. 25, p. 93–108.

———— 1991, A model for simulating transport of reactive multispecies components: model development and demonstration: Water Resources Research, v. 27, p. 3075–3094.

Zienkiewicz, O. C., 1977, The Finite Element Method, 3d edition: London, McGraw-Hill, 787 p.